Feasibility of Model-Assisted Probability of Detection Principles for Structural Health Monitoring Systems Based on Guided Waves for Fiber-Reinforced Composites

Kilian Tschöke, Inka Mueller, Vittorio Memmolo, Maria Moix-Bonet, Jochen Moll, *Member, IEEE*, Yevgeniya Lugovtsova, Mikhail Golub, Ramanan Sridaran Venkat, and Lars Schubert

Abstract—In many industrial sectors, structural health monitoring (SHM) is considered as an addition to nondestructive testing (NDT) that can reduce maintenance effort during the lifetime of a technical facility, structural component, or vehicle. A large number of SHM methods are based on ultrasonic waves, whose properties change depending on structural health. However, the wide application of SHM systems is limited due to the lack of suitable methods to assess their reliability. The evaluation of the system performance usually refers to the determination of the probability of detection (POD) of a test procedure. Up until now, only a few limited methods exist to evaluate the POD of SHM systems, which prevents them from being standardized and widely accepted in the industry. The biggest hurdle concerning the POD calculation is the large number of samples needed. A POD analysis requires data from numerous identical structures with integrated SHM systems. Each structure is then damaged at different locations and with various degrees of severity. All of these are connected to high costs. Therefore, one possible way to tackle this problem is to perform computer-aided investigations. In this work, the POD assessment procedure established in NDT according to the Berens model is adapted to guided wave-based SHM systems. The approach implemented here is based on solely computer-aided investigations. After efficient modeling of wave propagation phenomena across an automotive component made of a carbon-fiber-reinforced composite, the POD curves are extracted. Finally, the novel concept of a POD map is introduced to look into the effect of damage position on system reliability.

Index Terms—Acousto ultrasonics (AUs), automotive industry, damage detection, elastodynamic finite integration technique (EFIT), reliability assessment.

Kilian Tschöke and Lars Schubert are with the Department of Condition Monitoring and Test Services, Fraunhofer Institute for Ceramic Technologies and Systems IKTS, 01109 Dresden, Germany (e-mail: kilian.tschoeke@ikts.fraunhofer.de; lars.schubert@ikts.fraunhofer.de).

Inka Mueller is with the Institute of Mechanics, Bochum University of Applied Sciences, 44801 Bochum, Germany (e-mail: inka.mueller@hs-bochum.de).

Vittorio Memmolo is with the Department of Industrial Engineering, Università degli Studi di Napoli Federico II, 80125 Naples, Italy (e-mail: vittorio.memmolo@unina.it).

Maria Moix-Bonet is with the Institute of Composite Structures and Adaptive Systems, German Aerospace Center, 38108 Braunschweig, Germany (e-mail: maria.moix-bonet@dlr.de).

Jochen Moll is with the Department of Terahertz Photonics, Goethe University of Frankfurt am Main, 60438 Frankfurt am Main, Germany (e-mail: moll@physik.uni-frankfurt.de).

Yevgeniya Lugovtsova is with the Acoustic and Electromagnetic Methods Division, Bundesanstalt für Materialforschung und -prüfung (BAM), 12205 Berlin, Germany (e-mail: yevgeniya.lugovtsova@bam.de).

Mikhail Golub is with the Institute for Mathematics, Mechanics and Informatics, Kuban State University, 350040 Krasnodar, Russia (e-mail: m_golub@inbox.ru).

Ramanan Sridaran Venkat is with the Department of Non-Destructive Testing & Quality Assurance, Saarland University, 66125 Saarbrücken, Germany (e-mail: ramanan.sridaran@uni-saarland.de).

Digital Object Identifier 10.1109/TUFFC.2021.3084898

I. Introduction

IN THE field of structural health monitoring (SHM), an enormous amount of work, research, and development has been carried out for several decades. SHM is very attractive for many industry sectors, e.g., aerospace, automotive, and nuclear, allowing to increase safety and reduce operative costs by introducing a change in the maintenance philosophy. Nevertheless, there is still a gap between scientific research and the industrial deployment of various SHM methods. A main challenge for a broad application of SHM systems is the lack of suitable methods to assess their performance [1]–[3].

SHM systems are based on different physical principles adopted to detect the presence of damage. Examples are modal analysis, electromechanical impedance measurement, measurement of static parameters (strain measurement), methods of acoustic emission analysis, or methods based on elastic waves [4]. In particular, SHM methods based on elastic waves have been developed for a variety of industrial sectors. The focus of this work is on ultrasonic guided waves (UGWs), which are a special form of elastic waves guided by the boundaries of structures, such as plates and pipes. They are particularly suitable for damage detection because they are affected by the media through which they are traveling and are able to interact even with small hidden flaws, moreover allowing the inspection of inaccessible areas. Methods based
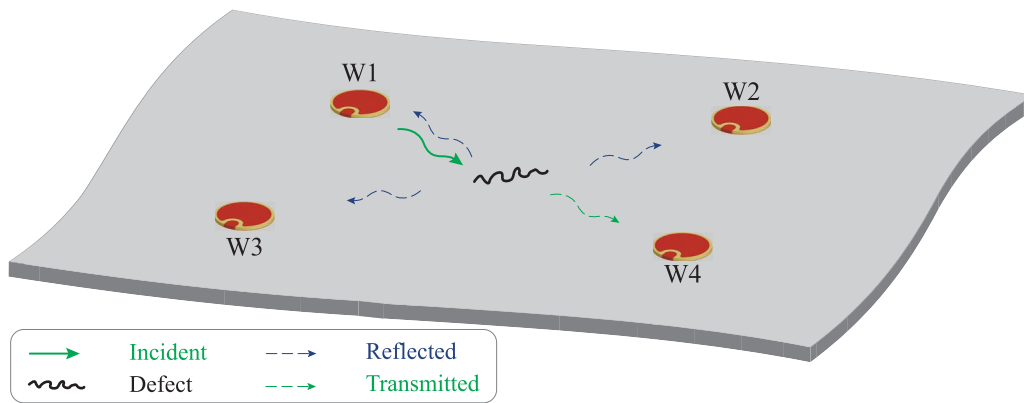
Fig. 1. Schematic drawing of a PZT-based guided waves SHM system on a free plate-like structure according to [14]. The system consists of PZTs (W1–W4), which can emit and receive ultrasonic signals. These signals interact with damage and can be partially reflected or transmitted.

on UGW are widely used, and specific approaches have been developed to detect various types of damage, such as delamination, holes, cracks, notches, corrosion, or the degradation of welded and riveted joints. A comprehensive summary and a basic description of these methods can be found in [5].

A schematic drawing of a guided wave-based SHM system on a plate-like structure is shown in Fig. 1. In the context of this explanatory example, W1–W4 are piezoelectric transducers (PZTs) attached to the structure. These transducers are able to emit and to receive elastic waves in the ultrasonic frequency range (20 kHz–1 GHz). If a transducer emits such a signal, it is called an actuator; if it records, it is called sensor or receiver. SHM methods based on ultrasonic signals actively excited by actuators are called acousto ultrasonic (AU) methods in the literature [6], [7]. They are further differentiated into those exploiting pitch–catch or pulse–echo measurements [8]. In the former, the actuator and sensor are different PZTs, and the focus is on the wave transmission through the damage, whereas the latter exploits the same transducer to excite and sense UGW focusing the attention on the flaw induced reflections. This work focuses on guided wave-based SHM systems using a pitch–catch configuration and a frequency of 225 kHz to detect damages in a composite structure. Over the years, many studies have shown the potential of guided waves to detect and localize damage in fiber composite structures proving their suitability for SHM of aerospace and automotive components [6], [9]–[13].

A known method to evaluate the performance of SHM systems consists in the determination of the probability of detection (POD) of a test method. In general, the POD can be understood as a probability curve, obtained by experiments or by simulations, which indicates the probability with which a fault can be detected [15]. The POD is usually a function of the size of a defect, which is represented in POD curves. The regulatory base for SHM is still on its way and with one issue being a lack of POD evaluation methods applicable for the reliability assessment of SHM systems [1]. Therefore, the development of POD methods for SHM systems is urgently required [3].

Since the transducers of an SHM system are permanently installed on a monitoring object, a purely experimental determination of the POD would involve a high experimental effort and an enormous amount of material. The need for numerical simulation to investigate and perform reliability assessment of such systems has been already pointed out in the literature [3]. Therefore, efficient and reliable simulation of the UGW propagation and their interaction with damage is a current research topic in the field of SHM [16]. Furthermore, various regulations, such as the SAE ARP 6461,[1] pave the way for computer-aided investigation of SHM systems. The reliable simulation of wave propagation phenomena is essential for this. That is why current research continues to deal with the efficient simulation of wave propagation phenomena. Thus, Gravenkamp *et al.* [18] write: "The simulation of wave propagation phenomena - even for linear two-dimensional cases - is still challenging for numerical methods. Particularly in the case of large domains (e.g., seismic waves) or short wavelengths (e.g., ultrasound) […]."

This work focuses on two main challenges regarding the reliability assessment of SHM systems. First, the POD is determined for a guided wave-based SHM system using simulated input data for a model-assisted POD (MAPOD). After obtaining the POD curves, the effect of the damage position on the system reliability is analyzed using a novel concept: the POD map.

This contribution is structured as follows. The introduction to SHM systems that have just been given is followed in Section II by a description of the concept of the POD as it is used in the field of nondestructive testing (NDT). It is followed by a section that shows why this approach has to be supported by numerical models for SHM systems. Afterward, Section III shows the governing equations of elastic waves and a selected discretization method. This method, known as the elastodynamic finite integration technique (EFIT), is specially adapted for the modeling of structures made of

---

[1]"SAE International is a global association of […] engineers and related technical experts in the aerospace, automotive, and commercial-vehicle industries" [17]. An Aircraft Recommended Practice is a guideline for developments in the aircraft industry.

carbon-fiber-reinforced composites. The procedure and parameters of the modeling are explained for a selected component from the automotive industry. In Section IV, the results of the numerical experiments are presented. Based on these results, a model-assisted concept for determining the POD of an SHM system is presented, which includes the visualization of system performance with the novel concept of so-called POD maps. The POD maps are finally discussed, and this work concludes with a summary in Section V.

II. PROBABILITY OF DETECTION FOR SHM SYSTEMS

This section starts with an overview of the available literature in POD, originating from classical NDT methods, and continues with the theoretical background for the calculation of the POD curves in SHM systems. Finally, the concept of MAPOD is presented.

A. Theory of POD

The POD indicates the probability of a system to detect a specific flaw [19]. The original development and description of the POD come from aviation and were driven by the high safety requirements in this industry. A historical overview can be found in [20]. The standards developed by Berens were used to determine the reliability of NDT methods used in regular inspections. Later, it was estimated that approximately 25% of an aircraft's operating costs are due to inspections and maintenance [9]. Therefore, the use of integrated monitoring methods, e.g., based on actively excited UGW, allows for structural evaluation and has the potential of replacing costly inspections.

Testing and monitoring methods must be qualified in accordance with the applicable test regulations to demonstrate a sufficiently high level of reliability in damage detection and assessment. This reliability assessment is based on the POD: a monotonous function of a parameter of interest, which characterizes the flaw [21], [22]. This parameter is usually the size of the flaw, and therefore, the POD is often given as a function of it [23]. In addition, critical flaw sizes that affect the integrity of the component during its lifetime are often known from the design. Therefore, a flaw of the critical size must be detected by a test procedure reliably so that the acceptance criterion can be met [24]. From this point, POD curves correlate each flaw size to the probability of detecting that flaw during the lifetime by the specified test procedure. The data to populate a POD curve can be obtained either by measurements or by numerical simulations, which must include information about the critical flaw and its size. From these diagrams, the $a_{90/95}$ value can be obtained. This value denotes the flaw size, which can be detected with a probability of 90% and a confidence level of 95% [25]. Practically, this flaw size represents quantitatively the performance of the inspection procedure, and the $a_{90/95}$ value is used to characterize the reliability of the system. A test system is considered suitable for the present test task if $a_{90/95}$ is smaller than the acceptance criterion.

Two parametric methods are mainly used to determine a POD in the field of NDT [9], [21], [26]. This is, on the one hand, a method based on binary data, the hit-miss analysis, and, on the other hand, the method of analysis of the signal response. The Berens method that is accepted as a standard can generally be categorized as a method of signal response analysis. The development from the hit-miss analysis through the analysis of the signal response to the Berens method is also described as an "evolution" of the POD calculation [27].

The standard work of POD determination in the field of NDT is the summary of various investigations in the aviation sector of the U.S. Department of Defense, from which a manual on the determination of the reliability of NDT systems was developed [28]. The manual, *MIL-HDBK* for short, and the associated software *mh1823* form an internationally accepted standard for performing POD analyses. The theoretical foundations on which the MIL-HDBK is based can be found in [23] and were later supplemented by Berens [26], Berens and Loomis [29], and Berens *et al.* [30]. These publications, in turn, form the basis for a large number of other works. A fundamental overview and an introduction to factors influencing POD can be found in [31]–[33]. However, a standard for carrying out POD investigations for SHM systems has not been established yet [1], [2], [4], [19], [34].

In the following, the Berens method is described, and the assumptions are discussed with regard to its application for the reliability assessment of SHM systems. Specifications within this work, which are made for the final application example, should be regarded as one way of implementation. The decisions made are based on existing research work and are intended to stimulate further scientific discussion.

The variables whose correlation is examined in POD observations are the damage size a and the signal response $\hat{a}$, also called damage index (DI). In the context of UGW, the DI is obtained from measurement signals after processing steps. A characteristic to describe the damage size depends on the application, the test procedure, and the type of damage. Possible characteristics are, for example, the flaw length, diameter, depth, area, or volume.

The basic assumption of the Berens method is a linear relationship between the damage size a and the DI $\hat{a}$. Under certain circumstances, this is only given in a semilogarithmic or double-logarithmic scale, i.e., the variables $\log a$ and $\log \hat{a}$ are included [28]. In the following derivation, the notations a and $\hat{a}$ are continued without loss of generality.

Remark 1 (Selection of a Suitable DI): Different guided wave modes interact differently with a certain type of damage [6]. Whether there is a linear relationship between damage size and DI depends, in particular, on the mode shapes of the stress components relative to the location of damage. A suitable DI shall, on the one hand, be adjusted to the type of damage, and on the other hand, it has to be demonstrated that it is linear with the damage size. A selection of possible damage indices is provided by Loendersloot *et al.* [10] and Su and Ye [35]. For anisotropic materials, e.g., fiber-reinforced composites, Buethe *et al.* [19] show the DI

$$DI = 1 - \|CC\| \qquad (1)$$

where CC describes the correlation coefficient and is linearly related to the area of a delamination on a logarithmic scale.

The cross CC is determined between the baseline and the current measurement.[2] Loendersloot *et al.* [10] and Moix-Bonet *et al.* [12], [13] examine a large number of DIs regarding their interaction with typical damage in composites. They ultimately identify four DIs that are optimally suited for the stated purpose. Among them is also the DI as given in (1). Based on these results from the literature, the DI based on CC is used in this work.

In general, the relationship between a and $\hat{a}$ can be described according to a linear model

$$Y = X \cdot \beta + \varepsilon \tag{2}$$

whereby the usual notation from statistics is used and with which

$$Y = \begin{pmatrix} \hat{a}_1 \\ \vdots \\ \hat{a}_n \end{pmatrix}, \quad X = \begin{pmatrix} 1 & a_1 \\ \vdots & \vdots \\ 1 & a_n \end{pmatrix}$$

$$\beta = \begin{pmatrix} \beta_0 \\ \beta_1 \end{pmatrix}, \quad \varepsilon = \begin{pmatrix} \varepsilon_1 \\ \vdots \\ \varepsilon_n \end{pmatrix}. \tag{3}$$

The vector of the dependent variable Y contains the DIs $\hat{a}_i$ for the associated damage sizes a_i determined after n measurements. The matrix X is called the data matrix or design matrix. β denotes the vector of the regression coefficients, and ε denotes the error vector, which describes external influences or measurement errors.

In the linear model, the following assumptions are still applied: the error components are independent and $\varepsilon \sim \mathcal{N}(0, \tau^2)$ applies, i.e., they are normally distributed with expected value 0 and have the identical variance τ^2. Under these assumptions, estimators b and ς^2 for β and τ^2, respectively, can be determined according to

$$b = (X^T X)^{-1} X^T Y$$

$$\varsigma^2 = \frac{1}{n}(Y - Xb)^T (Y - Xb). \tag{4}$$

In general, Berens *et al.* [23] use the maximum likelihood method to determine the estimators. Under the above conditions on ε, this coincides with the least-squares estimator presented in (4). With the estimator b, the regression line is determined as

$$\hat{a} = b_0 + b_1 a. \tag{5}$$

A flaw in the test object is accepted as detected if $\hat{a}$ exceeds a given threshold. This threshold is called decision threshold $\hat{a}_{\text{dec}}$. The larger the decision threshold, the larger is the smallest damage size that can be detected.

Remark 2 (Selection of the Decision Threshold): For SHM systems based on UGW, Loendersloot and Moix-Bonet [11] write that "no physical interpretation is available to set a general threshold." The reasons for this are the different wave

---

[2]In real laboratory measurements, the electronics may cause a phase shift between different time signals. To minimize the influence of this phase shift, the cross correlation coefficient can also be determined by the *Hilbert* transformations of the time signals. Since such a phase shift does not occur in simulations, the DI is determined directly from the time signals in the context of this work.

modes, reflections, mode conversions, and anisotropic behavior, the latter aspect being mainly valid for fiber composites. For real measurements, the decision threshold can be set at a level of 3 or 6 dB above the noise level. The noise level can be obtained from measurements of the reference state if multiple and statistically independent measurements are available. For this purpose, the baseline measurement must be repeated several times [14]. Usually, the inherent noise characterizing the signal response shows a normal distribution. When considering the specific metric (i.e., DI), it is possible to verify the normality assumption with a variety of parametric or nonparametric tests. Among them, the Kolmogorov–Smirnov test is certainly one of the most accepted and can be applied successfully even when a limited number of samples are available, such as in [36], where the satisfaction of the Gaussian assumption was achieved. If no noise level is known, as can be the case in simulations, it is possible to choose the decision threshold as the minimum of the regression line or to obtain it from attendant simulations [19]. In the present contribution, noise is inserted into the simulations. This is explained in Section III-B.

Since $\hat{a} \sim \mathcal{N}(X\beta, \tau^2)$, also

$$\hat{a}_{\text{dec}} = \Phi^{-1}(0.5, \text{Xb}, \varsigma^2) \tag{6}$$

applies, where Φ is the distribution function of the standard normal distribution. The POD(a) for the damage size a is defined according to

$$\text{POD}(a) = 1 - \Phi\left(\frac{\hat{a}_{\text{dec}} - (b_0 + b_1 a)}{\varsigma}\right). \tag{7}$$

Alternatively and according to Mueller [14], with the definition of

$$\mu_{\text{POD}} = \frac{\hat{a}_{\text{dec}} - b_0}{b_1}, \quad \tau_{\text{POD}} = \frac{\varsigma}{b_1} \tag{8}$$

(7) is rewritten as

$$\text{POD}(a) = \Phi\left(\frac{a - \mu_{\text{POD}}}{\tau_{\text{POD}}}\right). \tag{9}$$

That is, a given damage size a generates a DI $\hat{a}$, and the POD(a) is the probability that $\hat{a}$ exceeds the threshold $\hat{a}_{\text{dec}}$

$$\text{POD}(a) = P(\hat{a} > \hat{a}_{\text{dec}}). \tag{10}$$

The damage size for which POD(a_{90}) = 0.9 applies is denoted by a_{90} [26].

Since the determined POD curve is obtained from a specific sample, the real function can vary around the fit curve. For this reason, it is necessary to determine confidence bands around the POD curve in which the real function lies with the highest possible confidence level [15]. There are different approaches on the kind of confidence, such as tolerance bands, prediction bands, and confidence bands, which all return the degree of probability, belief, or support that an unknown parameter value lies in a specific interval. However, among those interval estimators, the latter one is the most commonly adopted. Although the amount of data available in MAPOD is countless and does not suggest the use of this approach, practical POD estimations are almost always made from data of limited sample sizes and, hence, require confidence bounds

to be given [37], motivating its use even in this context. There are various approaches in the literature for determining the confidence bands [15], [24], [27]. A comparison of different methods can be found in [38]. The derivation according to Berens can be found in [23] and [28]. The final resulting value $a_{90/95}$ specifies the flaw size a, which can be detected by measuring the DI $\hat{a}$ with a probability of 90% and a confidence level of 95% [14].

B. Model-Assisted POD

Influencing parameters that have been considered so far and implemented in models within the framework of the determination of a POD for classical NDT methods are the "human factor," the test conditions or environmental conditions, the test equipment (sensitivity, resolution), the test process, the material under investigation, or interactions between all the factors mentioned [33]. According to the conclusions emerging from the sixth European American Workshop on Reliability of NDE [39], influences can be broken down into four groups:

1) intrinsic capability;
2) environmental parameter;
3) human factors;
4) organizational factors.

However, influencing factors differ between NDT and SHM methods. For example, the "human factors" can be neglected when using an SHM system [40]. Furthermore, the limitation of environmental conditions with regard to integrated systems is not expedient since they should also be used in operation, i.e., under fluctuating environmental parameters. Environmental conditions, material properties, and the geometry of the objects under investigation can be identified as the cause for fluctuations in monitoring systems [2]. For SHM systems, the installation of the actuators and sensors on a structure and the distribution of the damage are further factors influencing the variations in damage detection [4]. The measurement results of an SHM system are usually closely related to the structure on which it is applied and, therefore, cannot be transferred to other structures [27]. The latter authors also consider the variability of damage, i.e., its position and orientation, as parameters influencing the POD of an SHM system. Furthermore, the probability of damage occurring and its distribution are often unknown in reality [27].

In summary, the verification of the POD for SHM systems requires not only a variation of failure types and sizes, as well as the geometry and structure of various coupons and components, but also the consideration of various environmental parameters. The effort and scope for tests to prove a POD are considerably greater for SHM systems compared to NDT methods and cannot be achieved by laboratory tests alone. As Buethe *et al.* [19] write: "due to the fixed mounting of SHM systems on structures, experimentally based investigation is particularly difficult and resource consuming." Investigations of the POD must, therefore, also be carried out based on simulations, also known as MAPOD. In the literature, MAPOD approaches are basically divided into two categories [2], [22], [27], [41].

1) *Transfer Function Method:* Empirically determined POD curves are used to obtain estimates of the POD

of a comparable inspection scenario. This means that empirical data from several individual experiments are combined to form an overall statement about the POD of an NDT method. During the determination of the new POD curve, it is argued how significant factors influence the POD. The influencing factors represent well-understood physical phenomena.

2) *Completely Model-Based:* With this approach, factors that cause fluctuations within an inspection are systematically modeled and their effects identified. The models are used to estimate signal responses and fluctuations.

Current research is initially concerned with the development and understanding of the POD concept in the context of SHM since there is no standard procedure for determining the POD of an SHM system [27]. This work follows a completely model-based approach.

III. NUMERICAL MODELING

In this work, the EFIT is used for modeling the wave propagation phenomena through an automotive component made of composite material. The EFIT method allows modeling the complete wave field in homogeneous and heterogeneous, isotropic, and anisotropic materials. Further details can be found in [42]–[45]. Section III-A lays the groundwork for the wave field modeling based on the EFIT and applies the method to the current test object.

A. Modeling of UGW in Anisotropic Materials

Cauchy's equation of motion describes the propagation of elastic waves in an (inhomogeneous) medium

$$\rho \frac{\partial^2}{\partial t^2} u = \nabla \cdot \sigma + f \tag{11}$$

with $\rho = \rho(x_1, x_2, x_3)$ being the mass density, $u = (u_1, u_2, u_3)$ the displacement vector, t the time, $\sigma = \{\sigma_{ij}\}_{i,j=1,2,3}$ the stress tensor, and $f = (f_1, f_2, f_3)$ the body forces, respectively. In the case of linear deformations, Hooke's law holds true

$$\sigma = C \cdot \eta \tag{12}$$

where η denotes the strain

$$\eta = \frac{1}{2}\left(\nabla u + (\nabla u)^{\mathrm{T}}\right) \tag{13}$$

and

$$C = \begin{pmatrix} C_{11} & C_{12} & C_{13} & C_{14} & C_{15} & C_{16} \\ & C_{22} & C_{23} & C_{24} & C_{25} & C_{26} \\ & & C_{33} & C_{34} & C_{35} & C_{36} \\ & & & C_{44} & C_{45} & C_{46} \\ & \text{symm.} & & & C_{55} & C_{56} \\ & & & & & C_{66} \end{pmatrix} \tag{14}$$

is the elasticity matrix for the case of anisotropic materials.

The basic idea of the EFIT is to perform an integration of the differential equations over a defined control volume. First, (11) and (12) are transformed into a first-order hyperbolic system by introducing the particle velocity $v = (\partial/\partial t)u$

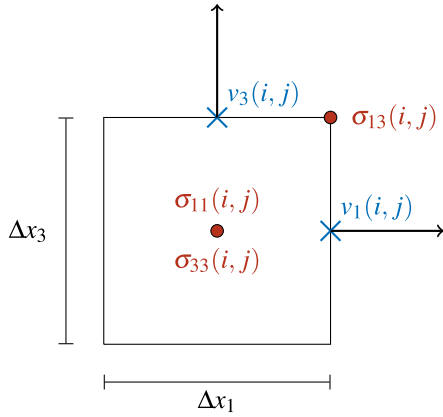$$\rho \frac{\partial}{\partial t} v = \nabla \cdot \sigma + f \tag{15}$$

Fig. 2. Staggered grid cell *i,j* of the 2-D-EFIT scheme.

and

$$\frac{\partial}{\partial t}\sigma = C \cdot \frac{\partial}{\partial t}\eta. \tag{16}$$

For readability, we present the method only for the 2-D case in the $x_1 - x_3$ planes and for the first component v_1 of (15). The exemplary equation is

$$\rho\frac{\partial}{\partial t}v_1 = \frac{\partial}{\partial x_1}\sigma_{11} + \frac{\partial}{\partial x_3}\sigma_{13} + f_1. \tag{17}$$

The integral form of (17) over such a control volume V reads

$$\int_V \rho\frac{\partial}{\partial t}v_1 \, dV = \int_V \left(\frac{\partial}{\partial x_1}\sigma_{11} + \frac{\partial}{\partial x_3}\sigma_{13} + f_1\right) dV. \tag{18}$$

With the help of the divergence theorem, we transfer (18) into

$$\int_V \rho\frac{\partial}{\partial t}v_1 \, dV = \int_V \left(\frac{\partial}{\partial x_1}\sigma_{11} + \frac{\partial}{\partial x_3}\sigma_{13} + f_1\right) dV \tag{19}$$

$$= \int_S (\sigma_{11}, \sigma_{13}) \cdot n \, dS + \int_V f_1 \, dV \tag{20}$$

where n is the outer unit normal vector of the boundary S. The most commonly used grid cells are Cartesian ones, and there are different possibilities to locate the unknowns within the control volume. Fig. 2 shows the staggered case often used for elastodynamic problems. Assuming the staggered spatial grid and applying the midpoint rule to the cell i, j we obtain a quadrature scheme from (19), which reads

$$\rho\frac{\partial}{\partial t}v_1(i, j) \cdot \Delta x_1\Delta x_3 = (\sigma_{11}(i + 1, j) - \sigma_{11}(i, j)) \cdot \Delta x_3$$
$$+ (\sigma_{13}(i, j) - \sigma_{13}(i, j - 1)) \cdot \Delta x_1$$
$$+ f_1(i, j) \cdot \Delta x_1\Delta x_3. \tag{21}$$

Dividing (21) by $\Delta x_1\Delta x_3$ results in

$$\rho\frac{\partial}{\partial t}v_1(i, j) = \frac{\sigma_{11}(i + 1, j) - \sigma_{11}(i, j)}{\Delta x_1}$$
$$+ \frac{\sigma_{13}(i, j) - \sigma_{13}(i, j - 1)}{\Delta x_3} + f_1(i, j). \tag{22}$$

For time integration, the Leap frog scheme is chosen to complete the EFIT procedure as follows:

$$v_1^{n+\frac{1}{2}}(i, j) = v_1^{n-\frac{1}{2}}(i, j) + \frac{\Delta t}{\rho\,\Delta x_1}\left(\sigma_{11}^n(i + 1, j) - \sigma_{11}^n(i, j)\right)$$

$$+ \frac{\Delta t}{\rho\,\Delta x_3}\left(\sigma_{13}^n(i, j) - \sigma_{13}^n(i, j - 1)\right)$$

$$+ \frac{\Delta t}{\rho}f_1^n(i, j). \tag{23}$$

Here, the upper index in v_1 and σ_{1k} corresponds to discretization in the time domain with time step Δt. The remaining equations of (15) and (16) are discretized employing almost the same procedure.

As boundary conditions, a stress-free boundary is assumed. This boundary condition is implemented with the help of the stress-imaging method. This technique is attributed to [46] and is described in detail in [47] and [48] for staggered grids.

B. Properties and Parameters of the Sample Application

In this work, test objects made of a carbon-fiber-reinforced plastic (CFRP) material are considered. The models are the result of work from the project *CarbonSafe*. The aim of this project was the development of a suitable SHM system for safety-relevant components made of CFRP in the automotive industry. More results of the project can be found in [49]–[51].

Modeling of the multilayered structure made of an anisotropic composite material is possible by EFIT if the elastodynamic material parameters of a single layer are known. Using a 3-D discretization of the structure, each ply can then be modeled as one or more material cells in the thickness direction. Since the single layers are usually thinner than $500\,\mu$m, the corresponding cells have a very small dimension in the thickness direction. To satisfy the stability condition of explicit time integration i.e., the Courant–Friedrichs–Lewy (CFL) condition, the time step of the overall algorithm becomes extremely small, which leads to a considerable computing time expenditure, especially when the number of layers increases. Although this approach would ensure high fidelity modeling of the structural behavior under transient dynamic load, the computational effort can be insufficient if the laminated plate has a certain number of plies. To reduce computational effort significantly, the multilayered material can be idealized by the equivalent single-layer (ESL) approach. This method has already been successfully used to model SHM systems based on UGW for composites [34]. In particular, it ensures a good computational efficiency without reducing the model performance. At the same time, it offers high accuracy in modeling of the global structure of the wave field [52] and returns reasonable indication about the interaction between wave and through thickness damage [34]. Originally, the ESL approach was developed and used for fatigue tests supported by finite element modeling on composite materials and is particularly suitable for thin laminate structures [53]. The aim of the method is to obtain a single layer, whose stiffness is equivalent to that of the multilayered material. The equivalent structure is obtained by computing the effective stiffness

matrix using the classical lamination theory, the first-order shear deformation theory, or other plate theories. They are derived by making suitable assumptions on the displacement of plate particles according to the shear behavior of the structure. Basic assumptions are given as follows.

1) Each individual layer is linearly elastic.
2) The laminate is very thin, i.e., the thickness is much smaller than the other dimensions.
3) The thickness is constant.
4) Due to the thin laminate, the plane stress condition holds true.

Another general condition for the validity of simplified plate theories concerns the wavelength, which shall be significantly greater than the structure thickness, this is usually the case for UGW whose wavelength is in the range of several tens of millimeters propagating in plate-like laminates of a few millimeters of thickness. Further explanations regarding plate theories and the propagation of Lamb waves in laminates can be found in [54]. Moreover, a detailed derivation of the effective stiffness matrix can be found in [55].

If the elastodynamic constants of a single layer and the stacking sequence of the laminate are known, the effective stiffness matrix can be calculated with the freely usable program eLamX^2, which is developed at the TU Dresden at the Institute of Aerospace Engineering. The program and an online manual describing the basic operation of $eLamX^2$ can be obtained from [56].

The automotive component made of CFRP is shown in Fig. 3. A CAD dataset of the geometry of the component was provided by the partner in the *CarbonSafe* project, which was used to extract the curvilinear edge of the component as a polygon. For the shown test specimen, the multilayered structure is given with the layup of [0/45/90/0/−45/90], whose equivalent elastic matrix is

$$C_{\text{ESL}} = \begin{pmatrix} 89.1 & 18.1 & 18.1 & 0 & 0 & 0 \\ 18.1 & 89.1 & 18.1 & 0 & 0 & 0 \\ 18.1 & 18.1 & 89.1 & 0 & 0 & 0 \\ 0 & 0 & 0 & 20.7 & 0 & 0 \\ 0 & 0 & 0 & 0 & 20.7 & 0 \\ 0 & 0 & 0 & 0 & 0 & 20.7 \end{pmatrix} \text{ GPa.} \quad (24)$$

Fig. 3 also shows a schematic drawing of the 2-D model of the test specimen, including the coordinate system. A total of four piezoelectric circular transducers were applied to the structure. Their centers are located at the positions

$$W1: x_1 = 80 \text{ mm}, \quad x_3 = 80 \text{ mm}$$
$$W2: x_1 = 240 \text{ mm}, \quad x_3 = 80 \text{ mm}$$
$$W3: x_1 = 150 \text{ mm}, \quad x_3 = 180 \text{ mm}$$
$$W4: x_1 = 300 \text{ mm}, \quad x_3 = 260 \text{ mm}.$$

In the ESL method, damage within the structure can be modeled as a local stiffness reduction. The damage idealization in a CFRP structure using the ESL method has already been described and investigated in the literature [57]. The degradation of the composite material can be modeled by reducing its stiffness according to

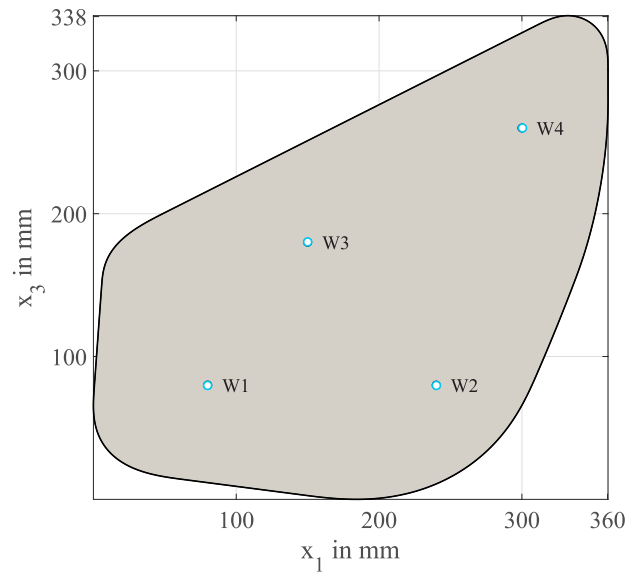$$\tilde{C} = \kappa \cdot C \quad (25)$$

Fig. 3. Top: picture of an automotive component made of CFRP. Bottom: schematic drawing of the 2-D model of the test specimen including marked positions of the PZTs (•).

where $\kappa = 0.5$ is the so-called scaling factor [57]. This assumption is supported by Dayal *et al.* [58]. Impact damages lead to microcracks in fiber composites, and these lead to a local reduction of stiffness. A corresponding approach within the framework of the ESL method was confirmed in [34] by experimental NDT measurements on a damaged test specimen.

In this work, the configuration of damage is varied, i.e., one damage is repeatedly introduced at one position and changed in form and orientation, leading to the introduction of variation, as it is necessary for the POD analysis. In general, impact-induced damage in composite materials can be assumed to be elliptical [19]. As part of the final reports of the SARISTU[3] project, different papers showed investigations on impact damage to structures made of composite materials in aircraft industry [10], [11]. The authors specify delaminations

---

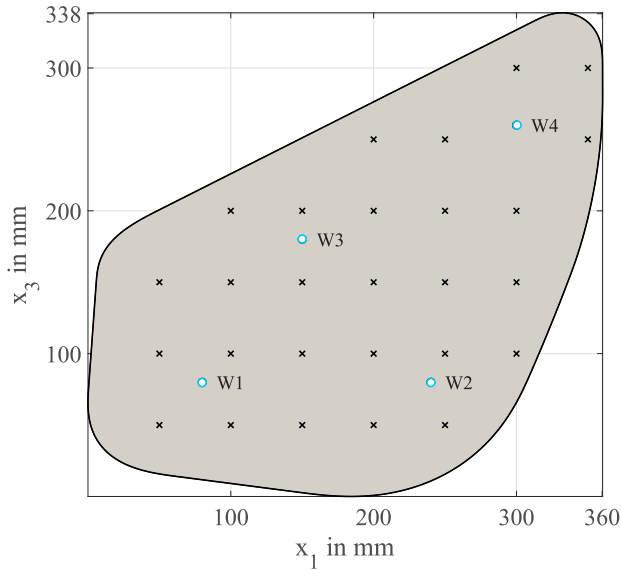[3]Smart Intelligent Aircraft Structures [59].

Fig. 4. Schematic drawing of the selected damage positions (×) and the positions of the PZTs (●) in the test specimen.

with a radius of more than 20 mm as critical because they lead to exterior damage barely visible by visual inspection. For the automotive sector, the publication of a corresponding specification is not known to the authors of this article. Therefore, a delamination area of 100 mm² is considered critical for the automotive CFRP component used in this study. This size is specified as the acceptance criterion for later examination.

The entire area to be discretized, which encloses the above-mentioned specimen from the *CarbonSafe* project, has an extension of 361 mm × 339 mm (see Fig. 4). The number of grid cells was 722 × 678 cells, resulting in $\Delta x = 0.5$ mm. Damage was modeled at 27 different locations shown in Fig. 4 in separate simulation runs. Each damage was modeled as a local change in stiffness according to (25) with $\kappa = 0.5$. The damage size a is the area A in mm². Starting from a given area, the damage was assumed to be elliptical with the semiaxes p and q. The semiaxes were randomly varied five times per given area A. A total of 11 different areas were specified for each damage position, from 50 to 150 mm² with an increase of 10 mm². First, the semiaxis p was determined, the length of which was normally distributed. The radius of a circle with an identical area A was assumed as the expected value μ. The standard deviation is defined by the following equation:

$$\tau = \frac{\mu - 3\Delta x}{3}. \tag{26}$$

Varying of damage orientation includes a variation of specific importance for the performance assessment based on the POD. With this specification, 99.73% of the values for p are in the interval $\mu \pm 3\tau$, and p is at least $3\Delta x$ long, i.e., it can be represented in the grid of discretization. From the value for p and $A = \pi pq$, q was finally determined. This procedure basically follows the investigations of [27], which considers the variability of damage as an influencing parameter on the POD of an SHM system. Other sources of variation, such

as the influence of environmental and operational conditions, such as stress and temperature, have not been taken into account in this purely simulation-based approach.

The transducers were modeled as a point source, whereas an actuator acted as surface forces f_1 and f_3 in both spatial directions, respectively. A five-cycle Hanning-windowed cosine pulse with a center frequency of 225 kHz was chosen as the excitation signal. For comparable structures and components, a damage interaction potential has already been shown in this frequency interval [49]. The observation time was set to 150 μs, which results in a total of 3600 time steps according to the CFL condition.

IV. RESULTS AND DISCUSSION

This chapter evaluates the performance of the formerly described guided wave-based SHM system by means of POD and is organized as follows. The wave field model, upon which the POD evaluation is based, is presented in Section IV-A. In Section IV-B, the POD curves for single combinations of actuator–sensor pairs and damage locations are determined. Section IV-C presents the POD maps as a method to display the POD evaluation for all damage locations. Finally, Section IV-D combines the POD maps to obtain the performance evaluation of the complete SHM system and analyzes the effect of the damage position on the system reliability.

A. Description of the Wave Field

Fig. 5 shows exemplary wave fields of the absolute value of the displacement in the test specimen at $t = 15$ μs and $t = 30$ μs, left and right figures, respectively. The transducer W1 was the actuator in this case. The baseline, the damage case with inserted damage with $A = 100$ mm², $p = 6.11$ mm, and $q = 5.2$ mm at the position $x_1 = 100$ mm and $x_3 = 100$ mm, and the difference signal of the two mentioned states are presented in Fig. 5. In the representations of the baseline and the damage case, the expected directional dependence of the wave field due to the anisotropy of the material is observed. The interaction with the damage can be seen more clearly when the difference signal is shown. The damaged area acts as a scatterer, and in addition, it can be seen how the scattered part of the wave also propagates directionally from the position $x_1 = 100$ mm and $x_3 = 100$ mm. These results correspond to the results of laser vibrometer measurements on comparable CFRP structures [6], [7].

B. POD Evaluation

To evaluate the POD of the SHM system, all transducers were used sequentially as actuators and the other three transducers as sensors. According to the pitch–catch approach, the transducer that is used as an actuator is not simultaneously adopted as the sensor. The DI in (1) is chosen to represent the signal response $\hat{a}$. In the literature, a linear relationship was shown for DI with the area of damage in anisotropic materials on double logarithmic axes [19].

The entire evaluation algorithm consists of determining the time signals of the baseline and the damage state at each sensor for each damage position, each damage size a, each
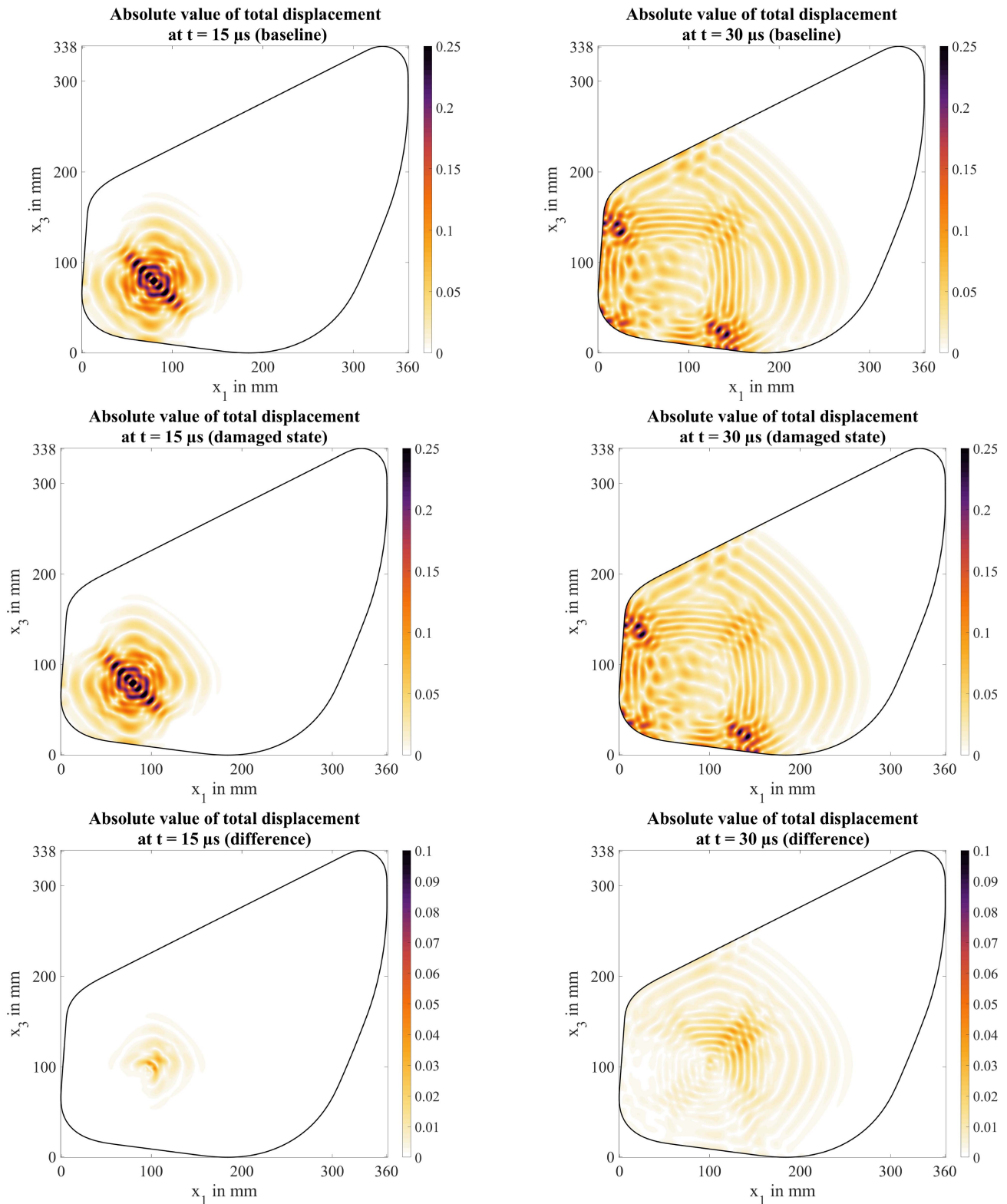
Fig. 5. Absolute value of the total displacement in the test specimen. The left and right columns show the wave fields at $t = 15$ μs and $t = 30$ μs, respectively. The upper row shows the baseline, and the middle row shows the damaged state with the damage introduced with $A = 100$ mm^2, $p = 6.11$ mm, and $q = 5.2$ mm at the position $x_1 = 100$ mm and $x_3 = 100$ mm. The bottom line shows the differential signal of the two states mentioned. The transducer W1 was the actuator.

damage configuration, and each actuator–sensor combination. This results in a total number of 5940 simulations. From the time signals, the DI $\hat{a}$ is calculated.

The decision threshold $\hat{a}_{\text{dec}}$ was obtained from the data of the simulations. The procedure was based on the method presented in [19]. The basic idea is that only the DIs on indirect
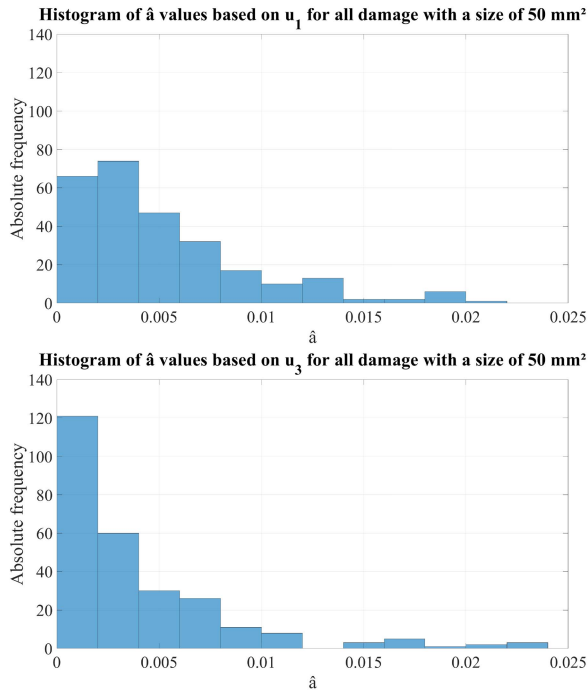
Fig. 6. Histograms of $\hat{a}$ values determined for the most distant pitch–catch paths for all damage positions and the smallest damage size of 50 mm². Top: when evaluating u_1. Bottom: when evaluating u_3.
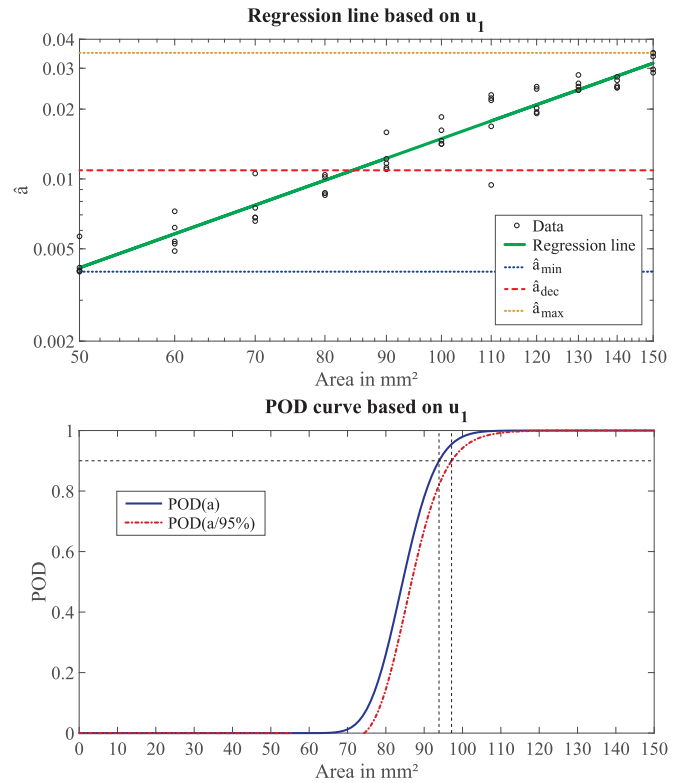
Fig. 7. Top: representation of the linear relationship between $\hat{a}$ and a including regression line and parameters of the investigation when evaluating the u_1 time signals. The transducer W1 was the actuator, and the transducer W2 was the sensor. The damage was located at the position $x_1 = 100$ mm and $x_3 = 100$ mm. Bottom: representation of the determined POD curve of a damage at the position $x_1 = 100$ mm and $x_3 = 100$ mm when evaluating the u_1 time signals. The values $a_{90} = 93.87$ mm² and $a_{90/95} = 97.14$ mm² were determined.

paths are evaluated to determine the decision threshold. Thus, only the DIs that are dominated by reflection components of the time signals are considered. For each damage position, the most distant pitch–catch path between two transducers was first determined. By the distance between a path and the damage position, the Euclidean distance between the location of the damage and the perpendicular foot on the path is meant. For this path, the DIs $\hat{a}$ were then determined for both actuator–sensor combinations for the five modeled damage sizes with $a = 50$ mm² according to (1). This resulted in a total distribution of 270 $\hat{a}$ values (see Fig. 6). From this distribution, the 90% percentile was chosen as the decision threshold. The evaluation of the time signals of the u_1 component resulted in $\hat{a}_{\text{dec}} = 0.0109$ and for the u_3 component in $\hat{a}_{\text{dec}} = 0.0087$. Based on these values, it can be assumed that the u_3 component is generally more sensitive and that considering the u_3 component will result in smaller values for a_{90} and $a_{90/95}$. However, later analysis shows that such a conclusion cannot be derived from the numeric value of the decision threshold.

The regression line between the damage size a and the DI $\hat{a}$ was then determined for each actuator–sensor combination. The POD curves according to Berens' model were then determined using the abovementioned specifications. Within the scope of the evaluation algorithm, two POD curves were generated for each damage position and each actuator–sensor combination: one based on the time signals of the u_1 component and one based on the time signals of the u_3 component. An example of the described evaluations is shown in Figs. 7 and 8. The following evaluations refer to the case of a damage at the position $x_1 = 100$ mm and $x_3 = 100$ mm. Fig. 7 shows the determined regression line between $\hat{a}$ and a based

on the time signals of the u_1 component for the actuator–sensor combination W1–W2. Since the damage position, in this case, is close to the actuator W1 (see Fig. 3), it can be expected that the influence on the time signals is relatively high, i.e., even very small damage should be detectable. Nevertheless, there are also a few outliers in Fig. 7, which can be related to the modeling of the damages. When defining the ellipses, one of the semiaxes was assumed to be normally distributed, and the second semiaxis was calculated from the area of the damage. The normal distribution of the semiaxes resulted in very narrow ellipses in a few cases. These ellipses, depending on the orientation between the damage and the wavefront, can lead to less or more interaction for the same size of the damage.

During the evaluation, the minimum and maximum of the $\hat{a}$ values were determined as $\hat{a}_{\text{min}} = 0.0040$ and $\hat{a}_{\text{max}} = 0.0349$, respectively. The resulting POD curve is also shown in Fig. 7, from which $a_{90} = 93.87$ mm² and $a_{90/95} = 97.14$ mm² were obtained. If the time signals of the u_3 component are evaluated, comparable values result with $a_{90} = 106$ mm² and $a_{90/95} = 109.18$ mm². Nevertheless, in this example, the u_1 component is more sensitive, i.e., more suitable for detecting the damage as one can see from the smaller values of a_{90} and $a_{90/95}$.
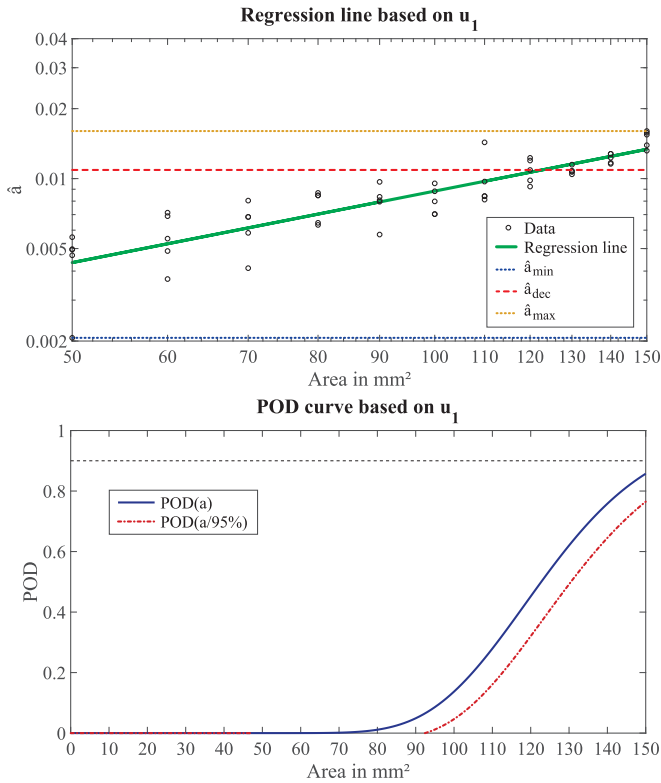
Fig. 8. Top: representation of the linear relationship between $\hat{a}$ and a, including regression line and parameters of the investigation, when evaluating the u_1 time signals. The transducer W3 was the actuator, and the transducer W4 was the sensor. The damage was located at the position $x_1 = 100$ mm and $x_3 = 100$ mm. Bottom: representation of the determined POD curve of a damage at the position $x_1 = 100$ mm and $x_3 = 100$ mm when evaluating the u_1 time signals. The values $a_{90} = 156.12$ mm^2 and $a_{90/95} = 168.56$ mm^2 were determined.

From the estimated POD, it is possible to obtain a_{90} for the defect size detectable with a 90% probability, which is standard accepted as safe. Taking into account the confidence interval, $a_{90/95}$ is obtained as the minimal defect size detectable with a 90% probability with a 95% confidence. This means that the defect size detected in 90% of cases has a 95% probability to be smaller than $a_{90/95}$. Many publications allude to the $a_{90/95}$ criteria for reliability, which is the flaw size at which POD is 90% with confidence of 95% or greater. Although $a_{90/95}$ has been criticized for its arbitrariness, it is the *de facto* metric for quantifying the performance of the system (the detectability criterion), giving that it represents the minimum detectable damage with a statistically meaningful belief. Nonetheless, for the sake of clarity, both a_{90} and $a_{90/95}$ are discussed afterward.

If, in contrast, the actuator-sensor combination W3–W4 is evaluated for the abovementioned damage position, the dependence of the POD on the location of the damage or on the arrangement of the transducers within the system becomes apparent. The damage position is no longer on a direct pitch–catch path between W3 and W4 (see Fig. 3). The difference signal at W4 is not dominated by the transmitted wave components but by those scattered from the damaged area. It is, therefore, to be expected that larger values for a_{90} and

$a_{90/95}$ will be retrieved for this actuator-sensor combination. Corresponding results based on the evaluation of the u_1 component are shown in Fig. 8. A smaller slope of the regression line compared to that in Fig. 7 can be observed. Parameters $\hat{a}_{min} = 0.0021$ and $\hat{a}_{max} = 0.0160$ were determined. If one compares the maximum $\hat{a}$ value of 0.0160 obtained in this case (W3–W4) with that of the actuator-sensor combination W1–W2 (0.0349), it becomes clear that the same damage sizes can result in different damage indices. From the constructed POD curve, $a_{90} = 156.12$ mm^2 and $a_{90/95} = 168.56$ mm^2 could be determined (bottom in Fig. 8). The flatter slope of the POD curve in Fig. 8 compared to that in Fig. 7 also confirms the preliminary consideration that larger defects must be occur for the actuator-sensor combination W3–W4 than for the combination W1–W2 to obtain a POD of 0.9. However, if the u_3 component is evaluated for the actuator-sensor combination W3–W4, $a_{90} = 50.5$ mm^2 and $a_{90/95} = 52.84$ mm^2 are obtained. The reflected part of the wave, which influences the difference signal and, thus, DI, dominates in the case of the u_3 component. This is, therefore, more suitable for the evaluation of the actuator-sensor combination W3–W4 in order to detect the above-mentioned damage.

It is worth noting that Fig. 7 shows a more heterogeneous scatter of data around the predicted value. However, the POD approach is based on certain strict assumptions about the regression model best fitting the data, which is demanded, as such, to accommodate the linear relationship between the signal response and the flaw size while ensuring a limited deviation of the signal response around the estimated value and the same deviation across all values of the flaw size. Nonetheless, the lack of homoscedasticity (homogeneous scattering) showed by some paths in the relationship between the response and flaw size will not alter the generality of the discussion made afterward and the qualitative validity of the results already shown (i.e., inspection be transducer pair W1–W2 will always return a performance much higher than that performed by W3–W4 when the damage is located at $x_1 = 100$ mm and $x_3 = 100$ mm). The use of the POD approach is, indeed, aimed to establish a rigorous way to evaluate how the damage position affects the performance of the system (measured by the path-based $a_{90/95}$) rather than to find out the more plausible $a_{90/95}$ value.

C. Creation of POD Maps

It has already been shown in the literature that the POD within an SHM network depends on the damage location [4], [60]. Since the PZTs of an SHM system are permanently installed, the distance between the transducers and damage varies depending on the location of the damage and, thus, also the POD. This effect is emphasized in anisotropic materials since their force-deformation behavior is directional and, thus, also the propagation speed of guided wave modes.

The influence of the chosen path between two transducers on the damage detection was investigated in [19]. Using numerical simulations on an anisotropic composite specimen, the authors show that a DI varies depending on the location within an SHM network. The numerical and experimental
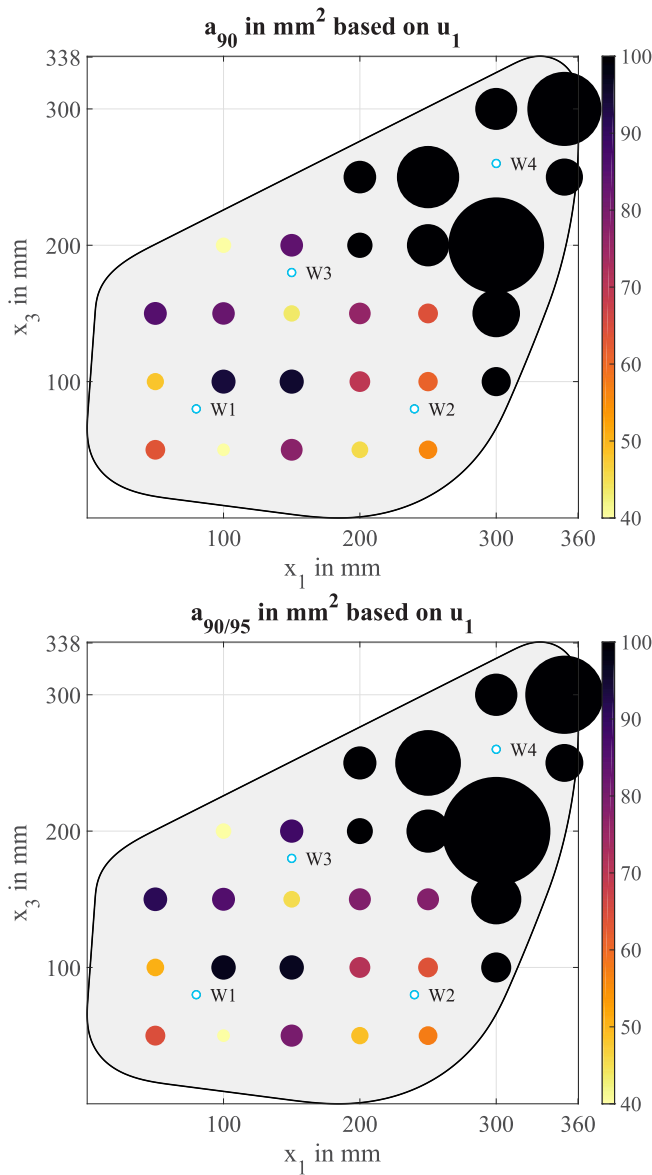
Fig. 9. Graphic representation of the determined a_{90} and $a_{90/95}$ values based on the evaluation of u_1. The transducer W1 was the actuator, and the transducer W2 was the sensor. Top: a_{90}. Bottom: $a_{90/95}$.

Fig. 10. Graphic representation of the determined a_{90} and $a_{90/95}$ values based on the evaluation of u_3. The transducer W1 was the actuator, and the transducer W2 was the sensor. Top: a_{90}. Bottom: $a_{90/95}$.

investigations in [4] also showed that the arrangement of the PZTs has an influence on damage detection. Since the location, size, and orientation of accidental induced damage are unknown in reality, the best possible arrangement of the transducers is also unknown. However, if the arrangement of the transducers within an SHM network is fixed, it follows that the location, size, and orientation of damage must be varied in order to assess the POD.

For this purpose, there is the possibility to create a POD map to investigate the influence of the damage location on the POD of an SHM system. A POD map is created by specifying a fixed number of points on the investigated object where damage is modeled. For each damage location, the size of the damage is varied, and the values a_{90} and $a_{90/95}$ are determined using the Berens method. This relationship can be visualized in a height profile map. Such maps based
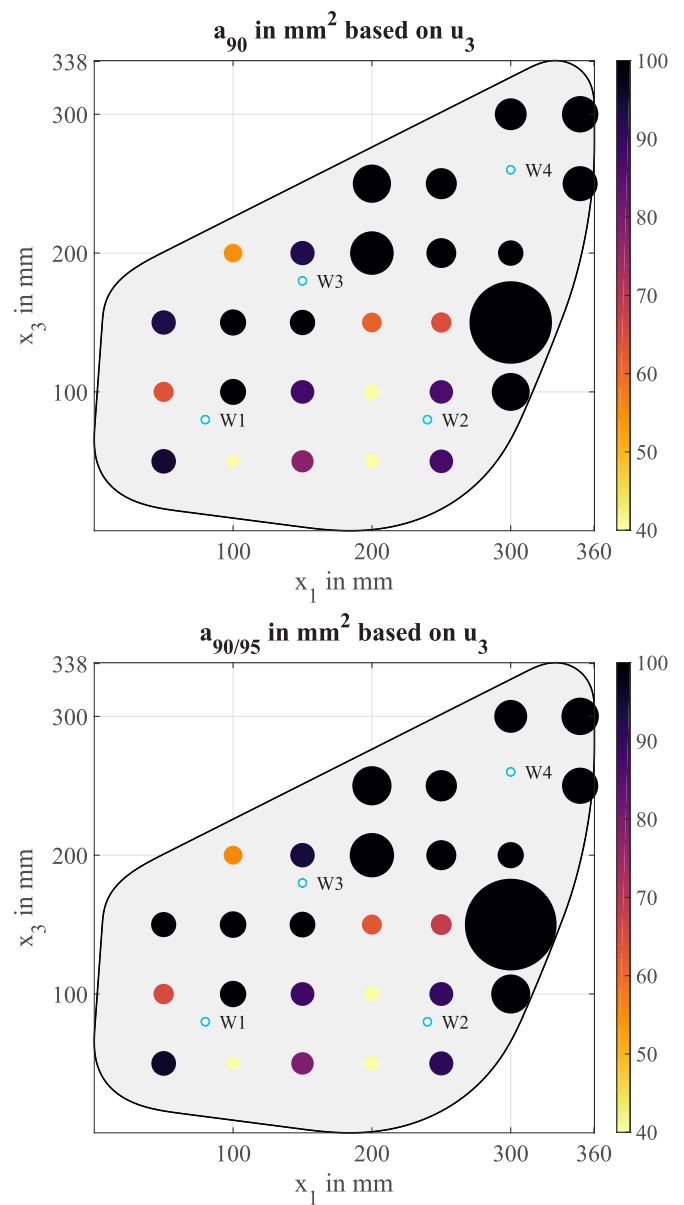
on computer-aided investigations of an SHM system were presented in [60] and [61].

The POD evaluation described in Section IV-B was then carried out for all damage positions. Figs. 9 and 10 show the determined a_{90} and $a_{90/95}$ values for the actuator–sensor combination W1–W2 when evaluating the u_1 and u_3 time signals, top and bottom, respectively. The damage positions that do not meet the acceptance criterion of $100\,\mathrm{mm}^2$ are marked in black. These representations also confirm the location dependency of the POD within the test specimen. In general, when evaluating the u_1 component, it can be determined that the acceptance criterion can be met in the area between W1, W2, and W3. This is not true in a region in the "Northeast" of the specimen (see Fig. 9). These damage positions are also not in the transmission path between W1 and W2. The magnitude of the DI
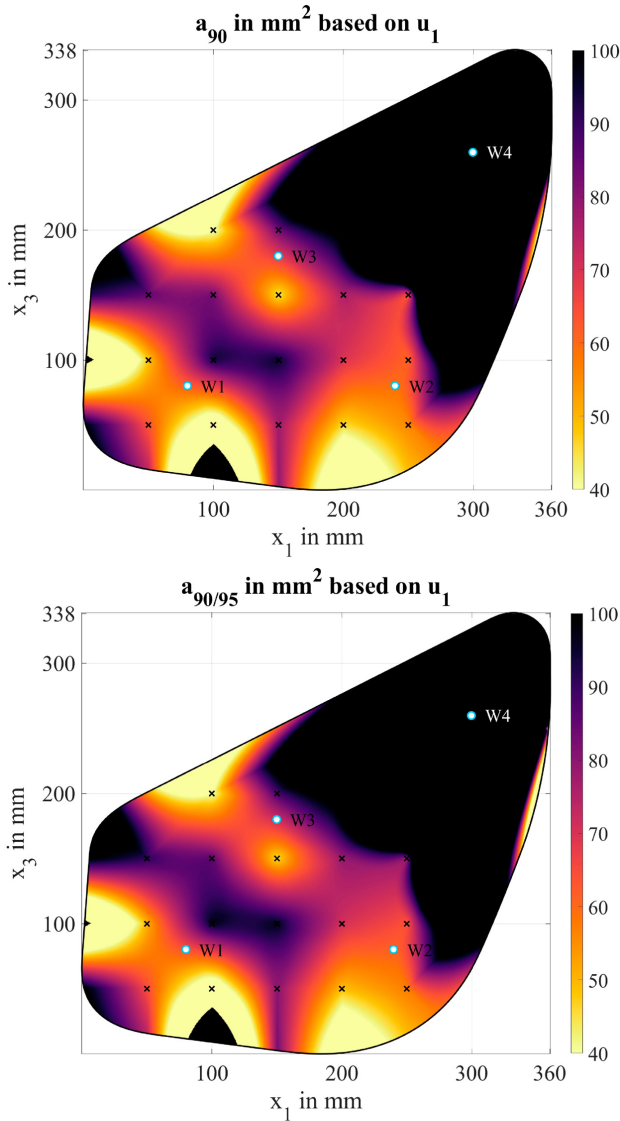
Fig. 11. POD maps obtained by interpolation from Fig. 9. The transducer W1 was the actuator, and the transducer W2 was the sensor. Top: a_{90}. Bottom: $a_{90/95}$.
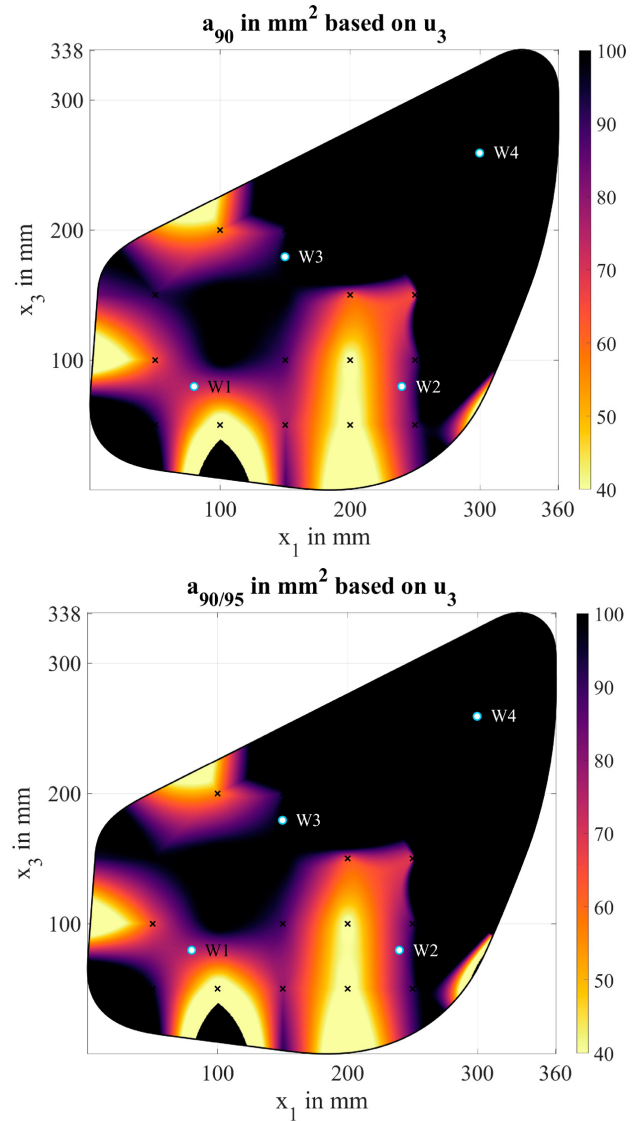
Fig. 12. POD maps obtained by interpolation from Fig. 10. The transducer W1 was the actuator, and the transducer W2 was the sensor. Top: a_{90}. Bottom: $a_{90/95}$.

is significantly influenced by the scattered wave component. However, this scattered wave only shows a clear influence on the u_1 differential signal at W2 at a high value of a. When evaluating the u_3 component, the determined a_{90} and $a_{90/95}$ values mostly decrease (see Fig. 10). Moreover, the acceptance criterion cannot be met for three damage positions within the region between W1, W2, and W3.

By interpolating the determined a_{90} and $a_{90/95}$ values from Figs. 9 and 10 to a finer grid, a POD map could be generated, respectively. The finer grid was chosen with a resolution of $\Delta x = 0.5$ mm. The MATLAB function *scatteredInterpolant* was used with the natural neighbor interpolation [62]. The results are shown in Figs. 11 and 12. These graphic representations once again illustrate the investigation of the actuator–sensor combination W1–W2 described above. The acceptance criterion can be met in the region between W1, W2, and W3, whereas this is not the case in the "Northeast" of the

test specimen. When evaluating the u_1 time signals, a maximum value of $a_{90/95} = 1910.58$ mm^2 could be determined among all damaged positions; when evaluating the u_3 time signals, a maximum value of 1318.38 mm^2 was determined.

In contrast, if the actuator–sensor combination W3–W4 is used, the POD maps change (see Figs. 13 and 14). In the region between W3 and W4, damage below the acceptance criterion of 100 mm^2 can now be detected. At the same time, this is not possible in areas in the "West," "South," and "East" of the test specimen, i.e., this actuator–sensor combination is also not suitable for globally meeting the acceptance criterion. Here, a local dependence of the POD is again confirmed. In general, the u_3 component of the displacement is more sensitive to damage. On the one hand, when evaluating the u_3 component, the determined a_{90} and $a_{90/95}$ values are lower in the region between W3 and W4; on the other hand, the acceptance criterion can be met in two areas around
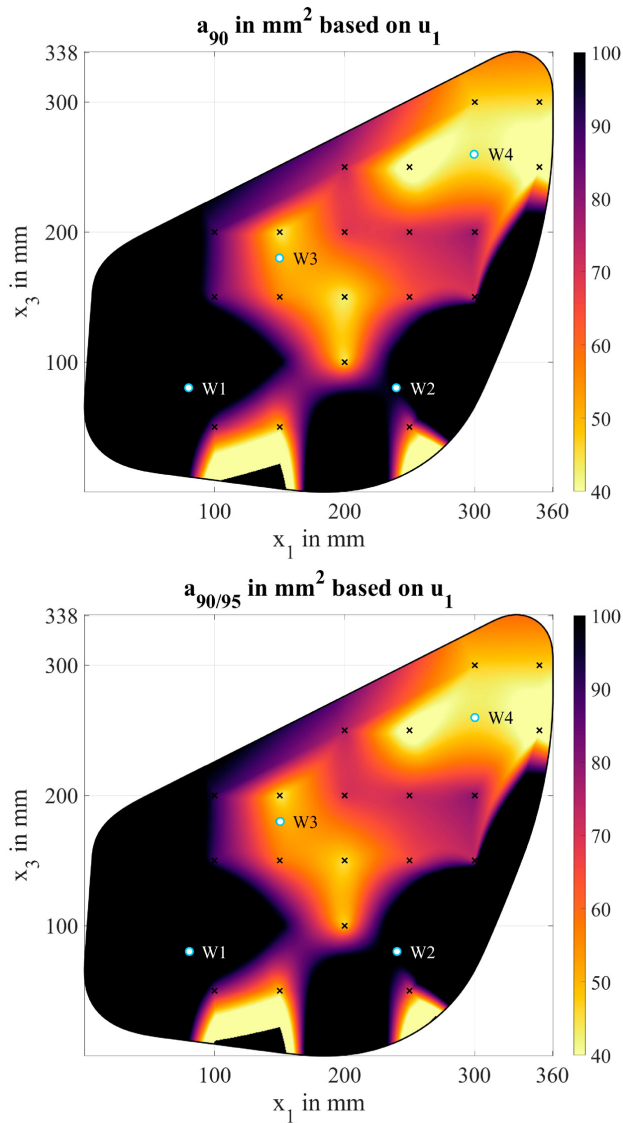
Fig. 13. POD maps obtained by interpolation based on evaluation of u_1. The transducer W3 was the actuator, and the transducer W4 was the sensor. Top: a_{90}. Bottom: $a_{90/95}$.
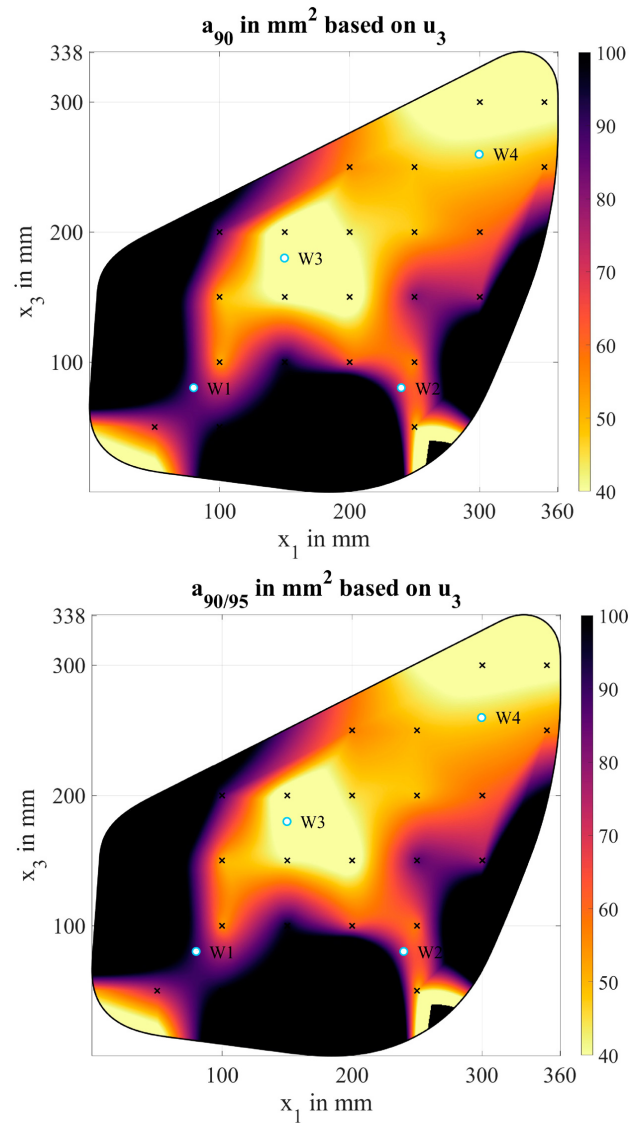

Fig. 14. POD maps obtained by interpolation based on evaluation of u_3. The transducer W3 was the actuator, and the transducer W4 was the sensor. Top: a_{90}. Bottom: $a_{90/95}$.

W1 and W2 (see Fig. 14). By evaluating the u_1 time signals, a maximum $a_{90/95}$ value of $333.28\,\text{mm}^2$ could be determined for the test specimen and, by evaluating the u_3 time signals, a maximum value of $252.33\,\text{mm}^2$.

D. Discussion

The preliminary investigations confirm that the POD within the SHM system depends on the arrangement of the transducers or the selected actuator–sensor combination. It follows that there is an optimal actuator–sensor combination for each damage position. In this context, optimal means that the actuator–sensor combination with the smallest a_{90} and $a_{90/95}$ value is selected. For example, the actuator–sensor combination W4–W1 was found to be optimal for the damage location at the position $x_1 = 100\,\text{mm}$ and $x_3 = 100\,\text{mm}$ with $a_{90} = 27.4\,\text{mm}^2$ and $a_{90/95} = 29\,\text{mm}^2$ when evaluating the u_1 component or $a_{90} = 30.62\,\text{mm}^2$ and $a_{90/95} = 31.9\,\text{mm}^2$

when evaluating the u_3 component. The order between the actuator and the sensor must be explicitly considered since the reciprocity on a pitch–catch path does not necessarily apply after damage has been introduced due to anisotropy. For the entire system, therefore, not only an optimal actuator–sensor combination can be specified for each damage position but also the component of the displacement that shows the higher interaction, i.e., the component where a_{90} and $a_{90/95}$ are smaller. In the example above, this is the u_1 displacement with $a_{90} = 27.4\,\text{mm}^2$ and $a_{90/95} = 29\,\text{mm}^2$.

Fig. 15 shows the a_{90} and $a_{90/95}$ values that are selected as optimal for all damage positions, among all actuator–sensor combinations, and between the components of the displacement. By interpolation of the determined a_{90} and $a_{90/95}$ values from Fig. 15, the POD map of the entire SHM system can finally be obtained (see Fig. 16). It can be seen that the entire system can meet the acceptance criterion of $100\,\text{mm}^2$,
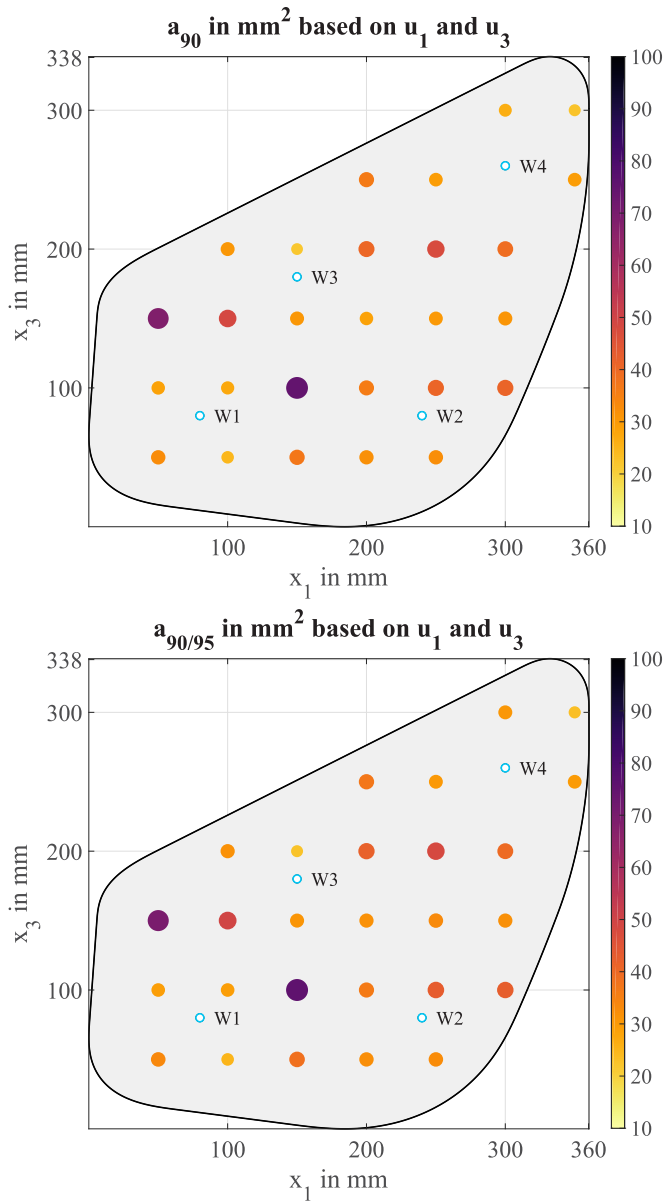
Fig. 15.   Graphic representation of the lowest a_{90} and $a_{90/95}$ values at the current damage positions among all actuator–sensor combinations. Top: a_{90}. Bottom: $a_{90/95}$.

Fig. 16.   POD maps obtained by interpolation from Fig. 15. Top: a_{90}. Bottom: $a_{90/95}$.

which does not apply to every actuator–sensor combination as one can see from the examples in Figs. 11–14. The maximum $a_{90/95}$ value of 75.59 mm^2 could be determined for the whole CFRP component. In a region in the "Northwest" of the test specimen and at $x_1 = 150$ mm and $x_3 = 100$ mm, only defects of the certain sizes can be detected with the needed probability, and other smaller damage will be missed. This result is particularly pronounced for the latter damage position, as it is located in a region between W1, W2, and W3 and is, nevertheless, difficult to detect. Due to the anisotropy of the specimen and the resulting characteristic of the wave propagation, it follows that the scattered wave field of this damaged area predominantly "passes" the transducers W1, W2, and W3 (see Fig. 5). Only a relatively large area of damage causes a reflected signal that is above the decision threshold.
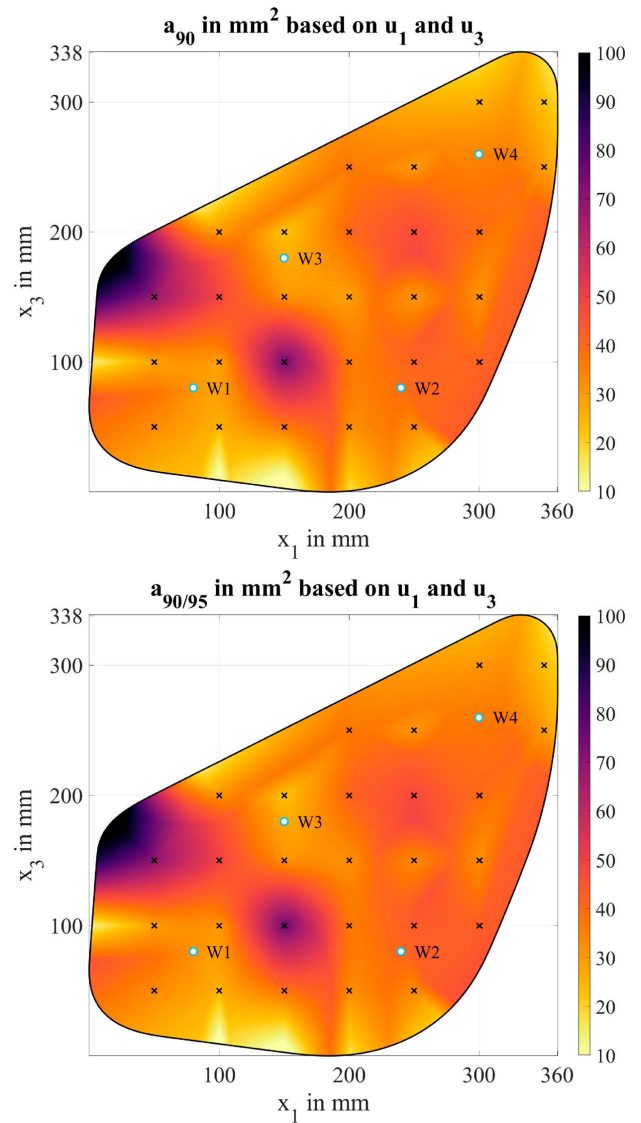
The structure of the distribution of the a_{90} and $a_{90/95}$ values with regions of smaller and regions of higher values that directly adjoin one another was also observed in the literature. Schubert *et al.* [60] visualized the maximum amplitude that can be achieved by constructive superposition of excited wave modes in a metal plate depending on the location. This maximum amplitude is directly related to a possible interaction with a damaged area and, thus, to the damage sizes that can be detected depending on the location. For anisotropic, plate-like structures made of fiber composite materials, Loendersloot *et al.* [10] and Memmolo *et al.* [34] show examples of imaging techniques used for damage detection. These examples also show that areas of high interaction can be located directly next to regions of less interaction. The causes are different distances between actuator, sensor, and damage position, as well as the anisotropic structure of the test object. Due to the purely model-based approach, the absolute values of POD curves and POD maps cannot be easily transferred to experimental investigations. On the one hand,

the determination of a decision threshold was realized using insensitive paths at the smallest modeled damage. Measurement noise was not taken into account due to the nature of the simulation. On the other hand, other influencing parameters, such as temperature variation or variation of stresses, have also not been included in the analysis. Moreover, the transducer itself has not been modeled. Instead, the resulting u_1 and u_3 components have been analyzed. Nevertheless, the qualitative statements of the study enable a highly improved knowledge about the system's performance. Especially, the POD map allows for a location-specific analysis of the system performance and enables SHM system engineers to make informed decisions during the design and operation phase.

V. CONCLUSION

In this work, the EFIT was used to model a curvilinear automotive component made of CFRPs. Furthermore, the ESL approach was used in the context of the discretization scheme to model the anisotropic material behavior of multilayered composites. These developments were then combined in order to check the feasibility of the MAPOD principle on the exemplary modeled automotive component. The approach for generating POD curves was taken from classical NDT and transferred to the modeled SHM system. To characterize the performance of the SHM system, a method for creating POD maps was presented and implemented. The results obtained visualize whether the SHM system is able to hold the acceptance criterion defined for the investigation. Nevertheless, a continuing comparison of the model and experimental data is still necessary to provide a complete reliability assessment of the SHM systems. The developments of this work can be used as tools for the model-assisted evaluation and optimization of an SHM system.

REFERENCES

[1] P. Cawley, "Structural health monitoring: Closing the gap between research and industrial deployment," *Struct. Health Monitor.*, vol. 17, no. 5, pp. 1225–1244, Sep. 2018.

[2] J. C. Aldrin, E. A. Medina, E. A. Lindgren, C. F. Buynak, and J. Knopp, "Protocol for reliability assessment of structural health monitoring systems incorporating model-assisted probability of detection (MAPOD) approach," Air Force Res. Lab., Comput. Tools, Gurnee, IL, USA, Tech. Rep. ADA585081, 2011.

[3] K. V. Jata, J. Knopp, J. C. Aldrin, and E. A. Medina, "Transitioning from NDE inspection to online structural health monitoring—Issues and challenges," in *Proc. 3rd Eur. Workshop Struct. Health Monitor.*, 2006, pp. 987–995.

[4] A. Gianneo, M. Carboni, and M. Giglio, "Feasibility study of a multi-parameter probability of detection formulation for a Lamb waves–based structural health monitoring approach to light alloy aeronautical plates," *Struct. Health Monitor.*, vol. 16, no. 2, pp. 225–249, Mar. 2017.

[5] J. L. Rose, "A baseline and vision of ultrasonic guided wave inspection potential," *J. Pressure Vessel Technol.*, vol. 124, no. 3, pp. 273–282, Aug. 2002.

[6] L. Schubert, U. Lieske, B. Köhler, and B. Frankenstein, "Interaction of Lamb waves with impact damaged CFRP's studied by laser-vibrometry and acousto ultrasonic," in *Proc. 18th Eur. Conf. Fract.*, Dresden, Germany, 2010, pp. 1–8.

[7] L. Schubert, U. Lieske, B. Frankenstein, and B. Köhler, "Interaction of Lamb waves with impact damaged CFRP's—Effects and conclusions for acousto-ultrasonic applications," in *Proc. 7th Int. Workshop Structural Health Monitor.*, 2009, pp. 151–158.

[8] V. Giurgiutiu, *Health Monitoring of Structural and Biological Systems*. New York, NY, USA: Academic, 2008.

[9] E. Monaco, V. Memmolo, F. Ricci, N. D. Boffa, and L. Maio, "Guided waves based SHM systems for composites structural elements: Statistical analyses finalized at probability of detection definition and assessment," *Proc. SPIE*, vol. 9438, Mar. 2015, Art. no. 94380M.

[10] R. Loendersloot, I. Buethe, P. Michaelides, M. Moix-Bonet, and G. Lampeas, "Damage identification in composite panels—Methodologies and visualisation," in *Smart Intelligent Aircraft Structures*. Cham, Switzerland: Springer, 2016, pp. 579–604.

[11] R. Loendersloot and M. Moix-Bonet, "Damage identification in composite panels using guided waves," in *Proc. 5th CEAS Air Space Conf.*, 2015, p. 14.

[12] M. Bonet, B. Eckstein, R. Loendersloot, and P. Wierach, "Identification of barely visible impact damages on a stiffened composite panel with a probability-based approach," in *Proc. 10th Int. Workshop Struct. Health Monit.*, 2015, p. 8.

[13] M. Moix-Bonet, P. Wierach, R. Loendersloot, and M. Bach, "Damage assessment in composite structures based on acousto-ultrasonics— Evaluation of performance," in *Smart Intelligent Aircraft Structures*, 2016, pp. 617–629.

[14] I. Mueller, "Inspection of piezoelectric transducers used for structural health monitoring systems," Ph.D. dissertation, Univ. Siegen, Siegen, Germany, Schriftreihe der Arbeitsgruppe für Technische Mechanik im Institut für Mechanik und Regelungstechnik—Mechatronik, 2017.

[15] C. A. Harding and G. R. Hugo, "Statistical analysis of probability of detection hit/miss data for small data sets," *Rev. Quant. Nondestruct. Eval.*, vol. 22, pp. 1838–1845, Mar. 2003.

[16] C. A. C. Leckey, M. D. Rogge, and F. R. Parker, "Guided waves in anisotropic and quasi-isotropic aerospace composites: Three-dimensional simulation and experiment," *Ultrasonics*, vol. 54, no. 1, pp. 385–394, Jan. 2014.

[17] SAE. (2019). *SAE International Deutschland*. [Online]. (Nov. 12, 2019). Available: https://de.sae.org

[18] H. Gravenkamp, A. A. Saputra, C. Song, and C. Birk, "Efficient wave propagation simulation on quadtree meshes using SBFEM with reduced modal basis," *Int. J. Numer. Methods Eng.*, vol. 110, no. 12, pp. 1119–1141, Jun. 2017.

[19] I. Buethe, N. Dominguez, H. Jung, C.-P. Fritzen, D. Ségur, and F. Reverdy, "Path-based MAPOD using numerical simulations," in *Smart Intelligent Aircraft Structures*. 2016, pp. 631–642.

[20] G. A. Georgiou, "Probability of detection (PoD) curves," Jacobi Consulting Ltd., London, U.K., Tech. Rep. 454, 2006.

[21] L. L. Gratiet, B. Iooss, G. Blatman, T. Browne, S. Cordeiro, and B. Goursaud, "Model assisted probability of detection curves: New statistical tools and progressive methodology," HAL, Tech. Rep. hal-01260335, 2016.

[22] R. M. Meyer, J. P. Lareau, S. L. Crawford, and M. T. Anderson, "Review of literature for model assisted probability of detection," Pacific Northwest Nat. Lab., Richland, WA, USA, Tech. Rep. PNNL-23714, 2014.

[23] A. P. Berens, *ASM Metals Handbook: Nondestructive Evaluation and Quality Control* (NDE Reliability Data Analysis), vol. 17. Materials Park, OH, USA: ASM International, 1988, pp. 689–701.

[24] M. Pavlovic, K. Takahashi, C. Müller, and R. Boehm, "NDT reliability— Final report: Reliability in non-destructive testing (NDT) of the canister components," Federal Inst. Mater. Res. Test., Swedish Nucl. Fuel Waste Manage. Company, Stockholm, Sweden, Tech. Rep. R-08-129, 2008.

[25] G. Jarmer and S. Kessler, "Probability of detection assessment of a guided wave structural health monitoring system," in *Proc. 10th Int. Workshop Struct. Health Monit.*, 2015, pp. 1–9.

[26] A. P. Berens, "Probability of detection (POD) analysis for the advanced retirement for cause (RFC)/engine structural integrity program (ENSIP) nondestructive evaluation (NDE) system-volume 1—POD analysis," Univ. Dayton, Dayton, OH, USA, Tech. Rep. AFRL-ML-WP-TR-2001-4010, 2000.

[27] A. Gallina, P. Packo, and L. Ambroziński, *Advanced Structural Damage Detection: From Theory to Engineering Application* (Model Assisted Probability of Detection in Structural Health Monitoring). Hoboken, NJ, USA: Wiley, 2013, pp. 57–72.

[28] *Nondestructive Evaluation System Reliability Assessment*, MIL-HDBK, Dept. Defense Handbook, Washington, DC, USA, 2009.

[29] A. P. Berens and J. S. Loomis, "Probability of detection (POD) analysis for the advanced retirement for cause (RFC)/engine structural integrity program (ENSIP) nondestructive evaluation (NDE) system development, volume 2—Users manual," Univ. Dayton, Dayton, OH, USA, Tech. Rep. AFRL-ML-WP-TR-2001-4011, 2000.

[30] A. P. Berens, W. Hoppe, D. A. Stubbs, and O. Scott, "Probability of detection (POD) analysis for the advanced retirement for cause (RFC)/engine structural integrity program (ENSIP) nondestructive evaluation (NDE) system development, volume 3—Material correlation study," Univ. Dayton, Dayton, OH, USA, Tech. Rep. AFRL-ML-WP-TR-2001-4012, 2000.

[31] L. Gandossi and C. Annis, "Probability of detection curves: Statistical best-practices," Eur. Netw. Inspection Qualification, LE Petten, The Netherlands, Tech. Rep. 41, 2010.

[32] D. S. Forsyth and J. C. Aldrin, "Build your own POD," in Proc. 4th Eur. Amer. Workshop Rel. NDE, Berlin, Germany, 2009, pp. 1–8.

[33] L. Schaefer, "Tutorial: POD basic," in Proc. 4th Eur. Amer. Workshop Rel. NDE, Berlin, Germany, 2009, pp. 1–88.

[34] V. Memmolo, F. Ricci, L. Maio, N. D. Boffa, and E. Monaco, "Model assisted probability of detection for a guided waves based SHM technique," Proc. SPIE, vol. 9805, Apr. 2016, Art. no. 980504.

[35] Z. Su and L. Ye, Identification of Damage Using Lamb Waves—From Fundamentals to Applications (Lecture Notes in Applied and Computational Mechanics), vol. 48. Berlin, Germany: Springer-Verlag, 2009.

[36] V. Memmolo, N. Boffa, L. Maio, E. Monaco, and F. Ricci, "Damage localization in composite structures using a guided waves based multiparameter approach," Aerospace, vol. 5, no. 4, p. 111, Oct. 2018.

[37] N. Nakagawa and R. B. Thompson, "Modelling ii model-assisted probability of detection: Use of nde models and statistical qualification of model predictions," in Proc. 7th Int. Conf. NDE Relation Struct. Integrity Nucl. Pressurized Compon., 2010, pp. 1–10.

[38] T. Sollier and C. Blain, "IRSN preliminary analysis on statistical methods for NDE performance assessment," in Proc. 12th Int. Conf. Destructive Eval. Relation Struct. Integrity Nucl. Pressurized Compon., Dubrovnik, Croatia, 2016, pp. 1–9.

[39] C. Mueller, M. Bertovic, D. Kanzler, and U. Ronneteg, "Conclusions of the 6th European American workshop on reliability of NDE," in Proc. AIP Conf., Berlin, Germany, 2016, pp. 1–10.

[40] P. Calmon, O. Mesnil, R. Miorelli, X. Artusi, B. Chapuis, and O. D'ALMEIDA, "Model assisted probability of detection for guided wave imaging structural health monitoring," in Proc. 4th Eur. Amer. Workshop Rel. NDE, Nov. 2019, pp. 811–816.

[41] C. Harding, G. Hugo, and S. Bowles, "Model-assisted probability of detection validation of automated ultrasonic scanning for crack detection at fastener holes," in Proc. 10th Joint Conf. Aging Aircr., 2007, pp. 16–19.

[42] P. Fellinger, R. Marklein, K. J. Langenberg, and S. Klaholz, "Numerical modeling of elastic wave propagation and scattering with EFIT—Elastodynamic finite integration technique," Wave Motion, vol. 21, no. 1, pp. 47–66, Feb. 1995.

[43] F. Schubert, A. Peiffer, B. Köhler, and T. Sanderson, "The elastodynamic finite integration technique for waves in cylindrical geometries," J. Acoust. Soc. Amer., vol. 104, no. 5, pp. 2604–2614, Nov. 1998.

[44] F. Schubert, "Numerical time-domain modeling of linear and nonlinear ultrasonic wave propagation using finite integration techniques—-Theory and applications," Ultrasonics, vol. 42, nos. 1–9, pp. 221–229, Apr. 2004.

[45] K. Tschöke and H. Gravenkamp, "On the numerical convergence and performance of different spatial discretization techniques for transient elastodynamic wave propagation problems," Wave Motion, vol. 82, pp. 62–85, Nov. 2018.

[46] A. R. Levander, "Fourth-order finite-difference P-SV seismograms," Geophysics, vol. 53, no. 11, pp. 1425–1436, Nov. 1988.

[47] P. Moczo, J. O. Robertsson, and L. Eisner, "The finite-difference time-domain method for modeling of seismic wave propagation," Adv. Geophys., vol. 48, pp. 421–516, Jan. 2007.

[48] J. O. A. Robertsson, R. Laws, C. Chapman, J.-P. Vilotte, and E. Delavaud, "Modelling of scattering of seismic waves from a corrugated rough sea surface: A comparison of three methods," Geophys. J. Int., vol. 167, no. 1, pp. 70–76, Oct. 2006.

[49] T. Gaul, K. Tschöke, E. Schulze, and L. Schubert, "Development and evaluation of structural health monitoring systems for fibre composites in automotive application based on elastic waves," in Proc. 9th Eur. Workshop Struct. Health Monitor., Manchester, U.K., 2018, pp. 1–10.

[50] K. Tschoke, T. Gaul, B. Weihnacht, and L. Schubert, "Modelling composites for structural health monitoring systems using acoustic ultrasonic methods," in Proc. 8th KMM-VIN Ind. Workshop Modelling Compos. Mater. Compos. Coat., 2018, pp. 1–20.

[51] K. Tschoke et al., "Development of an integrated measurement system for CFRP components within automotive manufacture," in Proc. 47th Nat. Conf. Nondestruct. Test. (KKBN), 2018, pp. 7–11.

[52] L. Maio, V. Memmolo, F. Ricci, N. D. Boffa, E. Monaco, and R. Pecora, "Ultrasonic wave propagation in composite laminates by numerical simulation," Compos. Struct., vol. 121, pp. 64–74, Mar. 2015.

[53] W. Van Paepegem and J. Degrieck, "Modelling strategies for fatigue damage behaviour of fibre-reinforced polymer composites," Eur. J. Mech. Environ. Eng., vol. 46, no. 4, pp. 217–227, 2001.

[54] A. Karmazin, "Time-efficient simulation of surface-excited guided Lamb wave propagation in composites," Ph.D. dissertation, Dept. Mech. Eng., Karlsruher Institut für Technologie, Fakultät für Maschinenbau, Karlsruhe, Germany, 2012.

[55] R. Glüge and J. Kalisch, "The effective stiffness and stress concentrations of a multi-layer laminate," Compos. Struct., vol. 111, pp. 580–586, May 2014.

[56] ELamX. (2018). Laminatberechnungsprogramm. Technische Universität Dresden, Institut für Luft- und Raumfahrttechnik. (Jul. 12, 2018). [Online]. Available: https://tu-dresden.de/ing/maschinenwesen/ilr/lft/elamx2/elamx

[57] S.-Y. Lee, G. Rus, and T. Park, "Detection of stiffness degradation in laminated composite plates by filtered noisy impact testing," Comput. Mech., vol. 41, no. 1, pp. 1–15, Sep. 2007.

[58] V. Dayal, V. Iyer, and V. K. Kinra, "Ultrasonic evaluation of microcracks in composites," in Advances in Fracture Research, vol. 5. Houston, TX, USA, 1989, pp. 3291–3300.

[59] SARISTU. (2017). Smart Intelligent Aircraft Structures. (Aug. 1, 2017). [Online]. Available: http://www.saristu.eu/

[60] F. Schubert, B. Frankenstein, M. Röllig, L. Schubert, and G. Lautenschläger, "Characterizing the performance of Lamb wave based SHM systems—A two-step approach based on simulation-supported POD and reliability aspects," in Proc. 5th Eur. Amer. Workshop Rel. NDE, Berlin, Germany, 2013, pp. 1–10.

[61] S. Venkat et al., "Optimized actuator/sensor combinations for structural health monitoring: Simulation and experimental validation," in Proc. Int. Workshop Struct. Health Monit., 2015, pp. 1014–1021.

[62] MathWorks. (2018) MATLAB Homepage. (Jul. 14, 2018). [Online]. Available: https://de.mathworks.com/help/matlab/ref/scatteredinterpolant.html

Kilian Tschöke received the Ph.D. degree in mathematics from the Technical University of Dresden, Dresden, Germany, in 2019.

Since 2011, he has been working with the Fraunhofer Institute for Ceramic Technologies and Systems IKTS, Dresden, initially as a Student Assistant and later as a Research Associate. He currently leads the Model-Based Data Evaluation working group for the computer-aided design of sensor systems. His fields of work include the modeling and simulation of elastic waves in complex, heterogeneous, and anisotropic materials, and the subsequent signal evaluation and statistical investigations on the quality of a monitoring system.

Inka Mueller received the Ph.D. degree in mechanical engineering from the University of Siegen, Siegen, Germany, in 2016.

After an intermediate step as a Junior Professor for structural health monitoring with Ruhr University Bochum, Bochum, Germany, she was appointed as a Professor for applied mechanics with the Bochum University of Applied Sciences, Bochum, in 2019. Her research is focused on wave-based and vibration-based SHM systems and their reliability.

Vittorio Memmolo received the B.Sc. and M.Sc. degrees in aerospace engineering and the Ph.D. degree in industrial engineering from the University of Naples Federico II, Naples, Italy, in 2012, 2014, and 2018, respectively.

He is currently a Post-Doctoral Researcher of aerospace structure with the Department of Industrial Engineering, University of Naples Federico II. During his early stage research career, he joined the Fraunhofer-Institut für Betriebsfestigkeit und Systemzuverlässigkeit LBF, Darmstadt, Germany, in 2017, and Goethe University Frankfurt, Frankfurt, Germany, in 2020, investigating several aspects of structural health and operation monitoring of mechanical structures and systems. His main research interests include guided wave-based SHM, load monitoring, measurements, mechanics of composites, and preliminary design of aircraft structures.

Maria Moix-Bonet received the joint master's degree in materials science and engineering from the Polytechnic University of Catalonia, Barcelona, Spain; the University of Lorraine, France; and Saarland University, Saarbrücken, Germany, in 2011.

In 2011, she joined the German Aerospace Centre, Braunschweig, Germany, where she is currently involved in the development of guided wave-based SHM for composite structures. Her interests are data-driven methods for damage identification and application-oriented development and testing of SHM systems.

Jochen Moll (Member, IEEE) received the Dipl.-Ing. and Ph.D. degrees in mechanical engineering from the University of Siegen, Siegen, Germany, in 2007 and 2011, respectively.

He is currently a Post-Doctoral Research Assistant with Goethe University Frankfurt, Frankfurt, Germany. His research interests include nondestructive testing, structural health monitoring, and signal processing techniques.

Yevgeniya Lugovtsova received the dual master's degree in nondestructive testing from Dresden International University, Dresden, Germany, and Tomsk Polytechnic University, Tomsk, Russia, in 2016.

Since 2016, she has been working as a Research Associate with Bundesanstalt für Materialforschung und -prüfung (BAM), Berlin, Germany. Her research interests are in the field of structural health monitoring with guided elastic waves and simulation using FEM.

Mikhail Golub received the Specialist degree in applied mathematics and computer sciences, and the Ph.D. and Habilitation degrees from Kuban State University, Krasnodar, Russia, in 2004, 2007, and 2016, respectively.

Since 2011, he has been a Principal Investigator with the Institute for Mathematics, Mechanics and Informatics, Kuban State University. His research interests lie in the area of computational mechanics and applied mathematics. In recent years, he has focused on wave propagation, acoustic metamaterials, and structural health monitoring.

Ramanan Sridaran Venkat received the Ph.D. degree in structural health monitoring using acoustic methods from Saarland University, Saarbrücken, Germany, in 2018.

Since 2010, he has been working with the Chair of Nondestructive Testing and Quality Assurance, Saarland University, where his core expertise is numerical modeling of nondestructive testing methods and data processing. He has participated in various DFG, European, and international research projects. He has more than 15 years of experience in NDT field.

Lars Schubert received the Ph.D. degree in electrical engineering from the Dresden University of Technology, Dresden, Germany, in 2011.

As part of his scientific research, he worked on the theoretical basis for the interaction of guided waves with damage in fiber composite structures. Since 2005, he has been working with the Fraunhofer Institute for Ceramic Technologies and Systems IKTS, Dresden, where he currently heads the Department of Condition Monitoring and Test Services. Since 2012, he has also been the Chairman of the Condition Monitoring Technical Committee of the German Society of Non-destructive Testing.